

# **SANDIA REPORT**

SAND98-0724

Unlimited Release

Printed March, 1998

## **FINAL REPORT OF LDRD PROJECT: ELECTROMAGNETIC IMPULSE RADAR FOR DETECTION OF UNDERGROUND STRUCTURES**

Guillermo Loubriel, John Aurand, Malcolm Buttram, Fred Zutavern, Darwin Brown, and Wesley Helgeson

Prepared by  
Sandia National Laboratories  
Albuquerque, NM 87185-1153  
for the United States Department of Energy  
under contract DE-AC04-94AL85000.

Issued by Sandia National Laboratories, operated for the United States Department of Energy by Sandia Corporation.

**NOTICE:** This report was prepared as an account of work performed by an agency of the United States Government. Neither the United States Government, nor any agency thereof, nor any of their employees, nor any of their contractors, subcontractors, or their employees, makes any warranty, express or implied, or assumes any legal liability or responsibility for the accuracy, completeness, or usefulness of any information, apparatus, product, or process disclosed, or represents that its use would not infringe privately owned rights. Reference herein to any specific commercial product, process, or service by trade name, trademark, manufacturer, or otherwise, does not necessarily constitute or imply its endorsement, recommendation, or favoring by the United States Government, any agency thereof or any of their contractors or subcontractors. The views and opinions expressed herein do not necessarily state or reflect those of the United States Government, any agency thereof or any of their contractors.

SAND 98-0724  
Unlimited Release  
PRINTED: March, 1998

Distribution  
Category UC-402, 403, 406

## **FINAL REPORT OF LDRD PROJECT: ELECTROMAGNETIC IMPULSE RADAR FOR DETECTION OF UNDERGROUND STRUCTURES**

Guillermo Loubriel, John Aurand, Malcolm Buttram,  
Fred Zutavern, Darwin Brown, and Wesley Helgeson  
High Power Electromagnetics Department  
Sandia National Laboratories  
P. O. Box 5800  
Albuquerque, NM 87185-1153

### Abstract

This report provides a summary of the LDRD project titled: Electromagnetic impulse radar for the detection of underground structures. The project met all its milestones even with a tight two year schedule and total funding of \$ 400 k. The goal of the LDRD was to develop and demonstrate a ground penetrating radar (GPR) that is based on high peak power, high repetition rate, and low center frequency impulses. The idea of this LDRD is that a high peak power, high average power radar based on the transmission of short impulses can be utilized effect can be utilized for ground penetrating radar. This direct time-domain system we are building seeks to increase penetration depth over conventional systems by using: 1) high peak power, high repetition rate operation that gives high average power, 2) low center frequencies that better penetrate the ground, and 3) short duration impulses that allow for the use of downward looking, low flying platforms that increase the power on target relative to a high flying platform. Specifically, chirped pulses that are a microsecond in duration require (because it is difficult to receive during transmit) platforms above 150 m (and typically 1 km) while this system, theoretically could be at 10 m above the ground. The power on target decays with distance squared so the ability to use low flying platforms is crucial to high penetration. Clutter is minimized by time gating the surface clutter return. Short impulses also allow gating (out) the coupling of the transmit and receive antennas.

A transmission line, charged to 100 kV, was discharged with high gain GaAs photoconductive semiconductor switches (PCSS) into a matched antenna. The design of the transmission line was based on calculations of the penetration of different electromagnetic waveforms produced by different pulser geometries. To this end, we developed a simple model that includes transmit and receive antenna response,

attenuation and dispersion of the electromagnetic impulses by the soil, and target cross sections. Thus, given an initial voltage waveform into the antenna, the program calculates the return waveform.

The system was used to: 1) measure penetration of the transmit pulse through large (2 feet thick) concrete blocks, 2) measure returns from targets in air (no penetration), 3) measure returns from targets obscured by concrete.

The enabling technology for the transmitter is high gain GaAs photoconductive semiconductor switches. These switches can hold off high voltages in the “off” state, and, when triggered with small laser diodes and laser diode arrays, have fast risetime, and low jitter. An important accomplishment of this LDRD is that we were able to trigger two switches, at opposite ends of a transmission line, with low enough jitter to achieve a bipolar waveform. At the start of tests, we only achieved a bipolar waveform once every 10 pulses. By the end of the LDRD we obtained very reproducible waveforms. This was achieved through a combination of multiple laser diode triggering and forcing the light to form lines on the switch instead of round spots that are the typical pattern from the optical fibers.

The specific Tasks/ milestones for FY96 and FY97 were:

Tasks/Milestones for FY96 and FY97:	Planned	Actual
Low voltage transmitter tests (including pulser/antenna coupling)	1/15/96	2/20/96
High voltage switch assembly and transmission line	12/1/95	4/9/96
Modulator capable of 100 kV, 1 kHz operation	2/15/96	3/15/96
Design a mask, procure GaAs wafers, and fabricate the PCSS	3/1/96	1/15/96
Design and build the receive antenna	4/1/96	12/1/95
Install diagnostics and laser diode array in the laboratory	4/1/96	3/29/96
Assemble the transmitter with laser diode and fiber	6/1/96	6/7/96
Pulse charge the pulser and test diagnostics	8/1/96	6/13/96
Assemble and calibrate receive antenna	10/1/96	1/6/97
Measure radiated pulse waveform	2Q 1997	4/23/97
Measure return waveform from target in air	3Q 1997	8/97
Measure return waveform from “buried” target	3Q 1997	9/97
Final SAND report	3Q 1997	3/98

## CONTENTS

Section

1.0	SUMMARY/ CONCLUSION	6
	1.1 GOALS AND TASKS	6
	1.2 RESULTS	6
	1.3 CONCLUSIONS	10
2.0	INTRODUCTION: HIGH GAIN GaAs SWITCHES	11
	2.1 HIGH GAIN GaAs SWITCHES	11
	2.2 DEVICE DESCRIPTION	11
	2.3 HIGH GAIN	13
	2.4 CURRENT FILAMENTS	14
	2.5 DEVICE LONGEVITY	15
3.0	CALCULATIONS OF GROUND PENETRATION	17
	3.1 MODEL OF ELECTROMAGNETIC GROUND PENETRATION	18
	3.2 RESULTS FROM THE MODEL	21
4.0	RADAR TRANSMITTER	22
	4.1 MODULATOR	22
	4.2 PULSE FORMING LINE	26
	4.3 LASER DIODE ARRAYS AND ELECTRONICS	29
	4.4 ANTENNA AND IMPEDANCE MATCHING SECTION	30
5.0	SYSTEM TESTS	35
	5.1 SYSTEM TESTS	35
	5.2 TESTS WITH UN-OBSURED TARGETS	38
	5.3 PENETRATION THROUGH CONCRETE	41
6.0	REFERENCES	43

## 1.0 SUMMARY/ CONCLUSION

This section summarizes the goals of this project, the tasks required to meet the goals as outlined in the original LDRD proposal, and the results and conclusions of the LDRD.

### 1.1 TASKS

The goal of the LDRD was to develop and demonstrate a ground penetrating radar (GPR) that is based on high peak power, high repetition rate, and low center frequency impulses. The task are:

**Task:**

Task 0—Calculations of electromagnetic penetration into soil and radar returns

Task 1--Low voltage transmitter tests (including pulser/antenna coupling)

Task 2--High voltage switch assembly and transmission line

Task 3--Modulator capable of 100 kV, 1 kHz operation

Task 4--Design a mask, procure GaAs wafers, and fabricate the PCSS

Task 5--Design and build the receive antenna

Task 6--Install diagnostics and laser diode array in the laboratory

Task 7--Assemble the transmitter with laser diode and fiber

Task 8--Pulse charge the pulser and test diagnostics

Task 9--Assemble and calibrate receive antenna

Task 10--Measure radiated pulse waveform

Task 11--Measure return waveform from target in air

Task 12--Measure return waveform from “buried” target

Task 13--Final SAND report

### 1.2 RESULTS

Task 0- Calculations of electromagnetic penetration into soil and radar returns: This task was added at the beginning of the project to improve on initial back-of-the-envelope calculations of system requirements. We developed a model for GPR in which we can vary the initial voltage pulse into the antenna, and includes the measured antenna transfer function, the transmission of the electromagnetic waves on entering (and exiting) soil, attenuation and dispersion by the soil (real soils with varying water content), and the cross section of the target. The model assumes normal incidence into soil and target. The model showed that high peak power impulses do penetrate into soils with some water content in such a way that targets buried down to 10 m could be detected.

Task 1- Low voltage transmitter tests: An existing antenna was tested at low voltages to determine its characteristics, especially at low frequencies. We used different techniques (frequency-domain and time-domain) to characterize both the input reflection and the transmitting/radiating performance of the antenna. The antenna acts as a derivative antenna almost exclusively. Its input match is best at 50  $\Omega$  and its transfer function has a

low frequency roll-off of about 70 MHz (meaning that the antenna does not radiate effectively below 70 MHz). For this reason we modified the design of the pulse forming line to have 50  $\Omega$  impedance and for it to produce a bipolar pulse with a 6.3 ns period (so that its peak spectral content is at 133 MHz). We also built and calibrated a voltage divider to measure the voltage wave into the antenna (at the feed point).

Task 2- High voltage switch assembly and transmission line: A pulse forming line which incorporates two PCSS and a capacitive voltage probe was designed and tested. The line is capable of producing either bipolar or unipolar pulse (of either positive or negative polarity) depending on whether two (bipolar) or one (unipolar) of the switches is triggered. As part of the pulse forming line we designed and tested a self-integrating capacitive voltage probe.

Task 3- Modulator capable of 100 kV, 1 kHz operation: Two modulators were designed, built and tested: one was an all solid state, SCR-based system and the other was a thyatron-based system. They were designed for 120 kV peak, 1 kHz repetition rate but the risetime of the solid state modulator was slower (about 4  $\mu$ s) compared to the thyatron system (~270 ns). Only the thyatron-based system was fully developed and optimized: risetime of 270 ns, peak voltage of 100 kV, and full width at half maximum (FWHM) of 425 ns. The modulator can run up to a repetition rate of 1 kHz. With the modulator connected to a pulse forming line directly, the switches would have to be fired at peak voltage. The current in the switch would have two components: the 6 ns duration discharging of the pulse forming line and the 300 ns low current bleed-through of the modulator. We have found that this low, long-duration current reduces switch longevity. To eliminate this problem we have used diode stacks between the modulator and the pulse forming line. The diode stack holds the voltage on the line even after the modulator's pulse is extinguished. Thus, when the switches are triggered, only the short duration current is produced. In this LDRD, we designed a diode stack capable of holding off 180 kV .

Task 4- Design a mask, procure GaAs wafers, and fabricate the PCSS: The high voltages required for this project called for the use of 1.5 cm gap GaAs switches. For preliminary tests at lower voltages, however, switches at other, smaller, gaps were also fabricated. These were all n-i-n switches manufactured at Sandia in the Thin Films and Brazing Department.

Task 5- Design and build the receive antenna: The receive antenna is a crucial part of this LDRD. Several antenna options were considered: a D-dot (derivative) sensor, a resistively-loaded replica antenna, a conical antenna, and a corner reflector receiver (to reduce cross-talk between the transmit and receive antennas). These antenna options were evaluated during the initial phase of the free field tests and we subsequently utilized the resistively loaded replica antenna.

Task 6- Install diagnostics and laser diode array in the laboratory: As pointed out in other tasks, we developed two voltage monitors to measure the voltage on the pulse forming

line and on the feed to the antenna. New laser diode array drivers were also built and shielded since previous drivers were found to be too susceptible to electro-magnetic interference from the pulser/ transmitter and we needed to assure that the lasers were not being triggered by the modulator or by the first triggering or ringing in the pulse forming line. At one point, jitter in the system was due to false triggering of the lasers.

Task 7- Assemble the transmitter with laser diode and fiber, **jitter experiments**: After the system was built we quickly discovered that we could not easily radiate a bipolar waveform with the PCSS. The problem was that only one or the other switch seemed to trigger even though both of them were being activated. At the start of tests, we only achieved a bipolar waveform once every 10 pulses. By the end of the LDRD we obtained very reproducible waveforms at every pulse. This was achieved through a combination of stronger laser diode triggering and using glass rods as cylindrical lenses to form lines on the switch instead of round spots that are the typical pattern from the optical fibers. The rods result in very prompt firing of the switches with jitter of less than a nanosecond. We also modified the timing of the trigger pulses to the two switches. Instead of firing all the lasers at the same time, we accounted for slight variations in trigger delay between the two switches by triggering one switch slightly earlier than the other one.

Task 8- Pulse charge the transmission line, test diagnostics, and **reduction of system ringing**: Once the modulator, pulse forming line and antenna were built and tested individually, the system was assembled and tested as a transmitter. At this time we observed that the system was producing late time ringing: the initial pulse that was sent from the pulse forming line to the antenna was not radiated in its entirety and part of it was reflected back to the pulse forming line and eventually radiated at late times. These later transmitted pulses are a problem when the receiver is placed adjacent to the transmitter antenna since the pulse that arrives from the target may be coincident in time with the late time ringing and may be masked by it. The reason for the ringing is due to frequency mismatch between the pulser (in the unipolar configuration) and the antenna. The unipolar waveform has peak frequency content at 0 Hz and the antenna is not an effective transmitter at frequencies below 70 MHz. Thus we expected to see ringing in the pulser-antenna system, but it did not necessarily have to be radiated. The radiated waveform shows that this ringing does result in a transmitted pulse with after pulses that last for about 200 ns. We reduced this late time ringing in two ways: 1) by using the bipolar waveform instead of the unipolar pulse which is more efficiently radiated by the antenna due to its higher frequency content and, 2) using an impedance matching section that connects the pulse forming line to the antenna with a smooth impedance transition.

Task 9- Assemble and calibrate receive antenna: Making measurements of antenna response characteristics in the VHF range is well known to be a difficult task. We tested a D-dot antenna and a resistively-loaded TEM horn. The D-dot antenna has good frequency response that extends to very low frequencies but it lacked sensitivity so that the data was too noisy. An alternative was to use the previously calibrated TEM horn. This antenna was built for transient/ time-domain receiving applications such as this one prior to this LDRD. It was designed to produce an output voltage proportional to the

incident field. It has a very low dispersion design, discrete resistor loading of the aperture to reduce late-time undershoot of the receiving impulse response, and a broadband matching section. It was calibrated by comparing its output with a precision D-dot receiving antenna (at Sandia) and using a time-domain monocone/ ground plane antenna range (at NIST by Dr. A. Ondrejka). It was designed to have a bandwidth of roughly 100 MHz to 7 GHz, but has an upper roll-off (-3 dB) frequency of only 2.75 GHz (adequate for these experiments). The pass-band of the receiving antenna has an effective height of 2.0 cm averaged over the ~75 MHz to 2 GHz range. Unfortunately, these calibration procedures were carried out at facilities which did not provide the most desirable information in the operating band of our pulser. Regardless, the low frequency roll-off of this antenna (75 MHz) is not as low as we would like (30 MHz). Given that the low frequency roll-off of the transmit antenna is 70 MHz, the roll-off of the receive antenna is barely acceptable.

Task 10- Measure radiated pulse waveform: The pulser-antenna system was set up on the East side of Building 963, in Area IV and we radiated following a protocol that meets the requirements of the Sandia Frequency Coordinator (Bob Weaver, 4914) by informing the Kirtland Frequency Surveillance Station (Al Okino, 846-5378) that we are about to radiate. Radiated waveforms were measured in a variety of configurations designed to mitigate ground effects to obtain the antenna pattern and the radiated fields as a function of distance. This was carried out with the bipolar waveform being fed into the antenna. The antenna pattern is highly directional. It was measured at a radius of 20 feet. The half power occurs at about +/- 18 degrees (full width at half maximum is 36 degrees). The electric field versus distance was measured and is 1.4 kV/m at 20 feet and 0.34 kV/m at 40 feet for a charge voltage of 12 kV. The deviation from a 1/r dependence shows that these data were not taken in the far field.

Task 11- Measure return waveform from target in air: We measured return waveforms from a 4' by 8' metal plate. The best results were obtained with the plate at 45 degrees relative to the direction of the oncoming electromagnetic wave and the receiver at 90 degrees. The total distance that the wave traveled was either 40 feet or 100 feet in separate experiments. This reduced the effects of antenna ringing relative to the case when the receive antenna was located alongside the transmit antenna.

Task 12- Measure return waveform from "buried" target: We measured penetration through concrete, and return waveforms from targets behind concrete walls. In the first case we placed a receiver behind large concrete blocks- 2 feet thick. In the second we placed a target behind the wall of building 963 and measured returns. In both cases measurable penetration/ signals were observed.

Task 13- Final SAND report: The final report was delayed because we collected data to the end of FY97 and the writing of the report was carried out in FY98.

### 1.3 CONCLUSIONS

The idea of this LDRD is that a high peak power, high average power radar based on the transmission of short impulses can be utilized effect can be utilized for ground penetrating radar. This direct time-domain system we are building seeks to increase penetration depth over conventional systems by using: 1) high peak power, high repetition rate operation that gives high average power, 2) low center frequencies that better penetrate the ground, and 3) short duration impulses that allow for the use of downward looking, low flying platforms that increase the power on target relative to a high flying platform. Specifically, pulses that are a microsecond in duration require (because it is difficult to receive during transmit) platforms above 150 m (and typically 1 km) while this system, theoretically could be at 10 m above the ground. The power on target decays with distance squared so the ability to use low flying platforms is crucial to high penetration. Clutter is minimized by time gating the surface clutter return. Short impulses also allow gating (out) the coupling of the transmit and receive antennas.

The system was used to: 1) measure penetration of the transmit pulse through large (2 feet thick) concrete structures, 2) measure returns from targets in air (no penetration), 3) measure returns from targets obscured by concrete. The results show the capability of the system to obtain appreciable penetration through concrete structures and to detect targets behind those structures. The attenuation of the electromagnetic wave through the high density concrete was only a factor of 2.8 at the low frequencies used.

## 2.0 INTRODUCTION: HIGH GAIN GaAs SWITCHES

### 2.1 HIGH GAIN GaAs SWITCHES

High gain PCSS offer switching improvements in voltage, current, rise time, jitter, optical activation, size, and cost. High voltage operation of conventional (linear) PCSS, is limited by optical trigger energy requirements, which are 1,000 to 100,000 times greater than those for high gain PCSS. To understand and develop high gain PCSS many experiments have been performed (for general references, see reference 1). In order to explain what are PCSS and to describe the state-of-the-art, the following paragraphs provide a brief description of some of these associated properties and issues: (1) general device description, (2) high gain, (3) current filaments, and (4) device longevity.

### 2.2 DEVICE DESCRIPTION

The GaAs switches used in this experiment are lateral switches (see figure 2.1) made from undoped GaAs of high resistivity  $>10^7 \Omega\text{-cm}$  and metallic lands that connect the switch to an energy source and a load. The metallic contacts provide either p or n doped regions. The simplest n contact is the ubiquitous Ni-Ge-Au-Ni-Au metallization. The p contacts are made from Au-Be. The insulating region separating the two contacts (the gap, in analogy to spark gaps) has a length that varies from 0.2 mm to 3.4 cm since higher switched voltages require a larger gap to avoid surface flashover. Because of high electric fields the switches were immersed in a dielectric liquid (Fluorinert®). Pulse charging of this configuration is typically required to reduce the surface flashover problem.

For the tests in this report, laser diode arrays were used to trigger the switch/ switches (see figure 2.2). Each array consisted of three laser diodes coupled to a 300  $\mu\text{m}$ - diameter fiber optic. Each array delivered about 1/2  $\mu\text{J}$  in 20 ns at about 880 nm to illuminate the switch. The final configuration utilized four arrays and fibers per switch. The wavelength of the laser diode arrays ranged from 870 to 880 nm.

Since the SNL discovery of a high gain switching mode in GaAs, these switches have been investigated for use in many high voltage applications such as: impulse and ground penetrating radar, switches for firing sets for weapons, as drivers for laser diode arrays to allow detection of objects through fog and smoke, and high voltage accelerators. PCSS offer improvements over existing pulsed power technology. The most significant are: 100 ps risetime, kilohertz (continuous) and megahertz (burst) repetition rates, scalable or stackable to hundreds of kilovolts and tens of kiloamps, optical control and isolation, and solid state reliability. Table I shows the best results obtained with the switches for various applications.

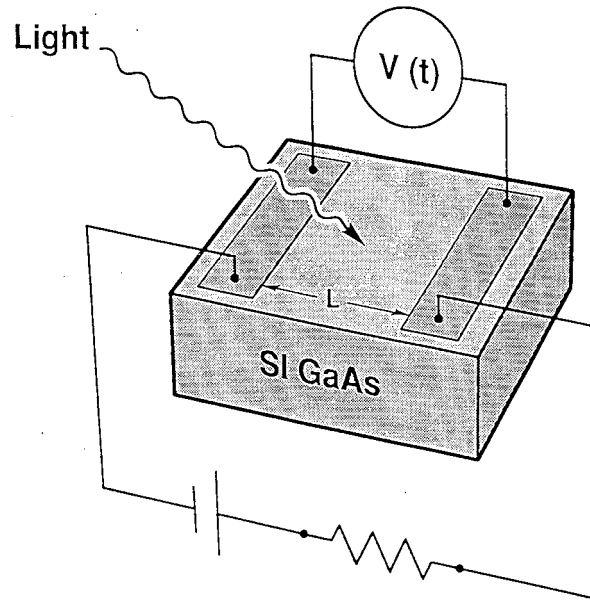


Figure 2.1. Schematic of the lateral semi-insulating (SI) GaAs switches used in this study. In this circuit the switch is being used to discharge a capacitor into a resistive load. The switch dimensions depend on the application. The distance between the contacts (the “gap,” in analogy to spark gaps) varies from 0.2 mm to 3.4 cm, for example. Switch thickness (the vertical direction) is always 0.6 mm.

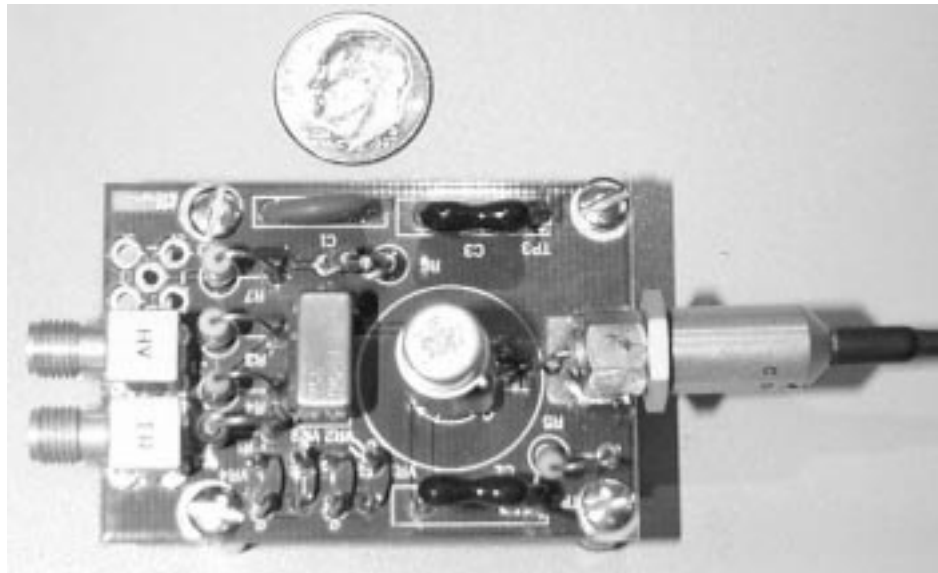


Figure 2.2. This close-up photograph shows the laser diode array, its electronics, and the optical fiber through which the laser’s output is taken to the PCSS. The laser diode is housed in the cylindrical section at the right. The connection of the optical fiber to the laser diode is barely visible at the right. To give an idea of size a dime is also shown.

In all the applications listed, the switch has been designed as a stand-alone system with a separate laser that triggers the switch. In a separate project we demonstrated that small lasers, capable of being monolithically integrated with the switch, did trigger the switch. This development, coupled with recent advances in switch lifetime/longevity, will allow rapid entry into new applications such as the one discussed here, ground penetrating radar.

<b>Table I</b> Parameter	GaAs, high gain mode, best individual results.	GaAs, high gain mode, simultaneous results.
Switch Voltage (kV)	200	100
Switch Current (kA)	7.0	1.26
Peak Power (MW)	120	48
Rise time (ps)	350	430
R-M-S jitter (ps)	80	150
Optical Trigger Energy (nJ)	2	180
Optical Trigger Gain	$10^5$	$10^5$
Repetition Rate (Hz)	1,000	1,000
Electric Field (kV/cm)	100	67
Device Lifetime (# pulses)	$>50 \times 10^6$	$5 \times 10^4$ , (at 77 kV)

Table I. Best switching results for high gain GaAs switches. The results in the first column are not simultaneous.

### 2.3 HIGH GAIN

Conventional PCSS produce only 1 electron-hole pair per absorbed photon. The energy of the individual photons excite electrons from the valence band to the conduction band. This excitation is independent of the electric field across the switch, and conventional PCSS can be operated to arbitrarily low voltage. High gain PCSS, on the other hand, occurs only at high electric fields (greater than 4 kV/cm). The photo-excited carriers, which are produced by an optical trigger, gain enough energy from the electric field to scatter valence electrons into the conduction band. This process is called impact ionization or avalanche carrier generation. Because many carriers are produced per absorbed photon, switches operating in this mode require extremely low energy optical trigger pulses, and they are called high gain PCSS in contrast to the conventional PCSS, which are often called linear PCSS. To stand off high voltage, PCSS must be made long enough to avoid avalanche carrier generation with no optical trigger (dark breakdown). The optical trigger energy for a linear PCSS scales with the square of its length. So high voltage linear PCSS can require rather high energy optical trigger pulses (25 mJ for 100 kV switches switched to 1  $\Omega$ ). It is the high gain feature of GaAs PCSS that allows their triggering with small semiconductor LDA. We have triggered 100 kV gallium arsenide (GaAs) PCSS, with as little as 90 nJ. A GaAs PCSS, operating in a low impedance circuit, can produce 100,000 times as many carriers as a linear PCSS would produce.

With most insulating materials (e.g. plastic, ceramic, or glass) and undoped semiconductors (e.g. silicon, gallium phosphide (GaP), or diamond), bulk avalanche carrier generation does not occur below 200 kV/cm. Semiconductors such as GaAs and indium phosphide (InP) are very different in that high gain PCSS can be initiated at unusually low electric fields (4-6 kV/cm and 15 kV/cm, respectively). Surface breakdown limits the field across PCSS to less than the bulk breakdown field (generally 100 kV/cm). Since PCSS need to absorb light through a surface, optically-activated avalanche breakdown is only practical in materials which exhibit high gain at lower fields (lower than the surface breakdown field). A very important part of the research into high gain PCSS has been to develop models for high gain at low fields in these materials.

Once avalanche carrier generation is initiated, it continues until the field across the switch drops below a threshold (4-6 kV/cm depending upon the type of GaAs). Since carrier generation causes the switch resistance to drop, in most circuits, the field across the switch will also drop. Indeed, when we first observed high gain PCSS, the most outstanding feature was that at high fields, when the switches would turn on, their voltage would drop to a constant non-zero value and stay there until the energy in the test circuit was dissipated. We originally called this switching mode “lock-on” to describe this effect. “High gain” has been adopted more recently to help distinguish this type of switching mode from other modes which also exhibit persistent conductivity, such as thermal runaway, and single or double injection. The field dependence for avalanche carrier generation that is exhibited in high gain PCSS is similar to that exhibited by Zener diodes. In series with a current limiting resistor, they will conduct whatever current is necessary to maintain a constant voltage across their contacts. In the case of a high gain PCSS, this voltage/field is the “lock-on” voltage/field or the threshold to low field avalanche carrier generation. The phase of switching during which the switch maintains this constant voltage drop is called the sustaining phase, and testing and modeling this phase is also a critical area of our research.

## 2.4 CURRENT FILAMENTS

Another important feature of high gain PCSS is that the current forms in filaments which are easily observed with a near infra-red sensitive camera (most non-intensified, black and white, CCD-based cameras). When the carriers recombine (i.e. conduction electrons drop back into the valence band), infra-red photons are emitted at approximately 875 nm (1.4 eV). If the filaments are near the surface of the switch, the emitted photons escape and they can be detected by a camera. Some images obtained in this manner are shown in figure 2.3. We believe that current filaments are fundamental to high gain PCSS and we have never observed high gain without current filaments. While current filamentation can lead to catastrophic destruction of the PCSS, current amplitude and pulse widths can be limited to allow non-destructive operation. In addition, the optical trigger can be distributed across the switch in a manner which creates multiple or diffuse filaments to extend the lifetime or current carrying capacity of the switch.

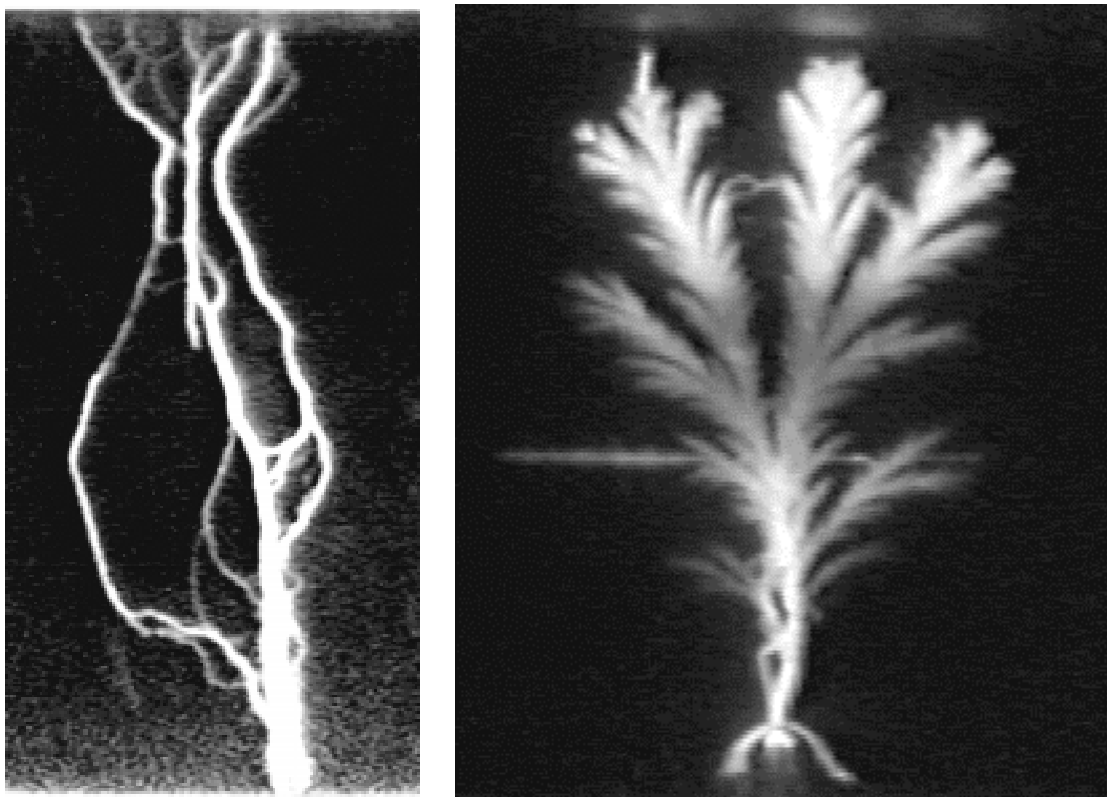


Figure 2.3. These photographs show examples of the current filaments which form during high gain PCSS operation. The images are recorded from the infrared (875 nm) radiation which is emitted as the carriers recombine in the switch. In both cases, the switches are 1.5 cm long (vertically). The PCSS on the left was charged to 45 kV and conducted 350 A for 10 ns. The PCSS on the right was charged to 100 kV and conducted 900 A for 1.4 ns.

## 2.5 DEVICE LONGEVITY

The biggest problem caused by the filaments is the gradual accumulation of damage at the contacts which limits their useful life to 1-10,000,000 shots depending upon the current per filament and the optical trigger distribution. Presently, device lifetime is a limitation of this technology for some applications. Although there is little change in performance, the PCSS degrade in time because the regions near the contacts are damaged on each pulse, and they gradually erode. The bulk semiconducting material shows very little, if any, degradation as the contact regions wear out. The fact that the degradation is confined to regions near the contacts suggests that substantial increases in switch lifetime can be made by developing better contacts that allow for higher current density. When this project started, high-gain PCSS would last for  $\sim 10^4$  pulses under a specific set of test conditions (0.5 MW). During the course of this project, the lifetime has been improved to  $5 \times 10^7$ . In comparison, the semiconductor lasers, which trigger or are driven by these switches, can last from  $10^8$  to  $10^{10}$  pulses. We are presently fabricating new generations

of deep-diffused and epitaxial-grown contacts that should yield further improvements. At higher powers or longer pulses, lifetimes are reduced. We plan to address these issues and accelerate lifetime testing by shifting our interests to higher current and higher repetition rate testing. Reference 2 describes our longevity experiments up to June of 1997.

The longevity tests have demonstrated that there is less contact degradation with short duration currents. In our longevity test-bed we utilize a pulse charger that charges a transmission line to high voltage with a risetime of about 1  $\mu$ s and a total pulse width of a few microseconds. If we discharge this transmission line when the charger is at full voltage, the switches will carry a current of 10 to 50 A for the length of the transmission line (3 to 30 ns, typically) and a much smaller current for a few microseconds. This long duration "recharge current" greatly reduces device life when compared to the case when the current only lasts for tens of nanoseconds. We determined this by adding isolation diodes between the pulse charger and the transmission line. When the line was charged, the isolation diodes would hold the line at high voltage. We would trigger the switches well after the pulse charger finished, thus discharging only the transmission line. These isolation diodes were also used in this LDRD.

### 3.0 CALCULATIONS OF GROUND PENETRATION

The ability of high gain GaAs photoconductive semiconductor switches (PCSS) to deliver high peak power, fast risetime pulses when triggered with small laser diode arrays makes them suitable for their use in radars that rely on fast impulses. This type of direct time domain radar is uniquely suited for observation of large structures under ground because it can operate at low frequencies and at high average power. This section will discuss the use of PCSS use in a radar transmitter. We will also present a summary of an analysis of the effectiveness of different pulser geometries that result in transmitted pulses with varying frequency content. To this end we developed a simple model that includes transmit and receive antenna response, attenuation and dispersion of the electromagnetic impulses by the soil, and target cross sections.

The system we are building seeks to increase penetration depth over conventional systems by using: 1) high peak power, high repetition rate operation that gives high average power, 2) low center frequencies that better penetrate the ground, and 3) short duration impulses that allow for the use of downward looking, low flying platforms that increase the power on target relative to a high flying platform. Specifically, chirped pulses that are a microsecond in duration require (because it is difficult to receive during transmit) platforms above 150 m (and typically 1 km) while this system, theoretically could be at 10 m above the ground. The power on target decays with distance squared so the ability to use low flying platforms is crucial to high penetration. Clutter is minimized by time gating the surface clutter return. Short impulses also allow gating (out) the coupling of the transmit and receive antennas.

The feasibility of using GaAs switches to create voltage pulses suitable for driving UWB antennas was demonstrated in a project in 1992- 1993 (see reference 3). In that study we charged a nominally 1.0 ns long, 47  $\Omega$ , parallel plate transmission line to voltages of about 100 kV. This line was discharged with either one or two switches into a 30  $\Omega$  load (see Figure 3.1). The voltage on the line rose to a peak value (100 kV in most cases, on occasion 110 kV) with a risetime of 210 ns. At peak voltage the laser diode arrays activated the switch and the line voltage dropped. The laser diode arrays (with most of their electronics) are about 2" by 2" in size and triggered the switches with as little as 90 nJ of energy.

If only one switch was triggered, the resulting load voltage was a unipolar pulse (of positive or negative polarity depending on which switch was triggered). The highest current obtained was 1.26 kA with a rise time of 430 ps and a pulse width of 1.4 ns. The peak power is 48 MW. This (1993) system operated in bursts of up to 5 pulses at a repetition rate of 1 kHz.

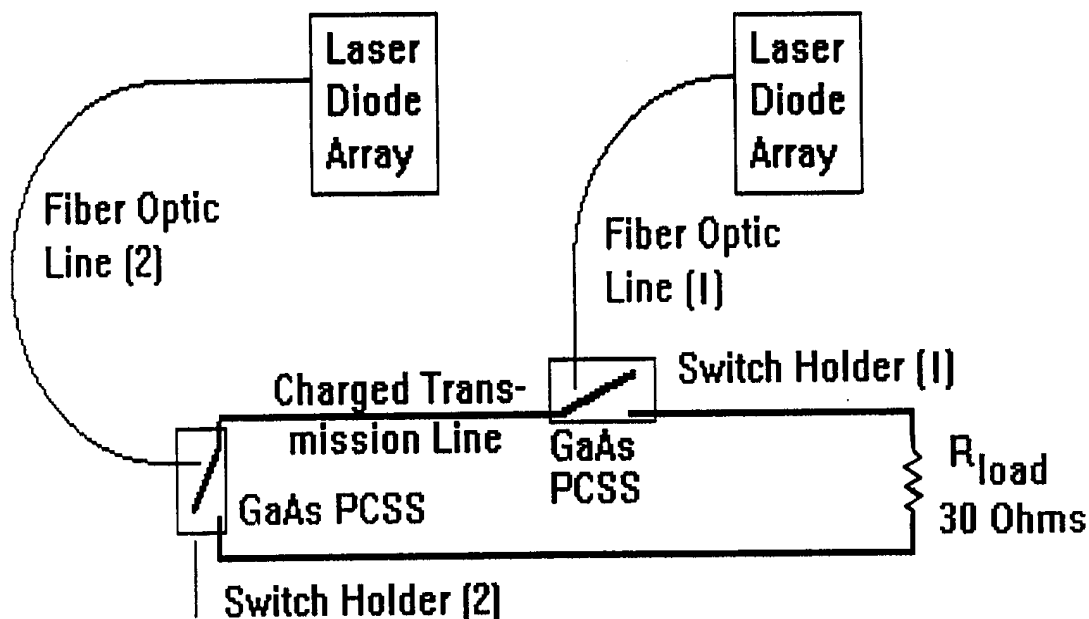


Figure 3.1. A short (1 ns), 47  $\Omega$  transmission line (the charge line) was charged to high voltage at a burst repetition rate of 1 kHz. Two switches were used on either side of the line to discharge the line into a 30  $\Omega$  or 50  $\Omega$  load.

The second set of tests carried out in 1993 used both laser diodes, one per switch, to produce a bipolar pulse. In theory, with ideal switching, the bipolar pulse should be composed of two unipolar pulses of opposite polarity each with half the pulse width. Thus, we expect a bipolar pulse composed of a negative and a positive pulse, each with a width of 0.9 ns. What we observe is a width of 1.0 ns for the negative pulse and 1.3 ns for the positive pulse. The reason for this is a timing error of about 200 ps. The minimum width should occur when both switches are triggered simultaneously. It is very important to trigger both switches at the same time to obtain full voltage and to obtain the proper waveform. In these tests, the switch jitter did not allow us to always reproduce the bipolar pulse. To reduce jitter it was deemed necessary to increase the laser energy (as was eventually done in this project).

Thus, results prior to this LDRD show that we can generate unipolar or bipolar pulses but that it was very difficult to obtain the latter. At the start of this LDRD we decided to calculate the expected electromagnetic returns from buried targets from unipolar and bipolar waveforms to see if we could get by with an unipolar waveform.

### 3.1 MODEL OF ELECTROMAGNETIC GROUND PENETRATION

To analyze the relative merits of different waveforms (unipolar versus bipolar) with varying frequency content and to estimate the peak powers required for a given soil

penetration, we have developed a simple radar model. This model (see references 4 and 5) includes transmit and receive antenna response, attenuation and dispersion of the electromagnetic impulses by the soil, and target cross sections. The target that we will choose is a metallic, square plate of size  $L$  buried at a depth  $D$ . To examine the radar equation for a buried object, we use the simple radar equation for the frequency dependent amplitude of the transfer function [radar-to-target-to-receiver]. The beam is assumed to be normal to the ground which is flat and featureless. Figure 3.2 shows two different voltage waveforms (input to antenna) that we will discuss in the paper: a unipolar pulse and a bipolar pulse. The formulas used to calculate these waveforms are either a Gaussian ( $\sigma = 0.8$  ns) centered at 5 ns or a Gaussian times  $(t - 5$  ns). Both were normalized to peak amplitude of 1 (as shown). These waveforms were meant to mimic the results obtained with the previous impulse system.

The frequency spectrum of both of these waveforms, shown in figure 3.3, is what determines their penetration characteristics. The unipolar pulse, due to its non zero integral, has peak frequency content at 0 MHz (dc). Most of its energy content is from 0 MHz to about 200 MHz. The bipolar pulse, on the other hand, has no frequency content at 0 and peaks at 200 MHz. Most of its energy content is from 100 MHz to 350 MHz.

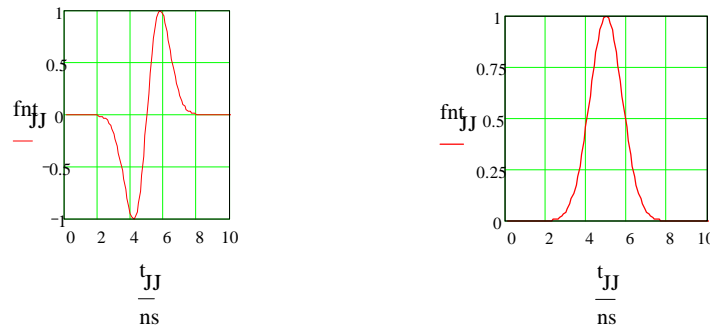


Figure 3.2. Voltage waveforms used in this study. On the left is a bipolar pulse, on the right is a unipolar pulse.

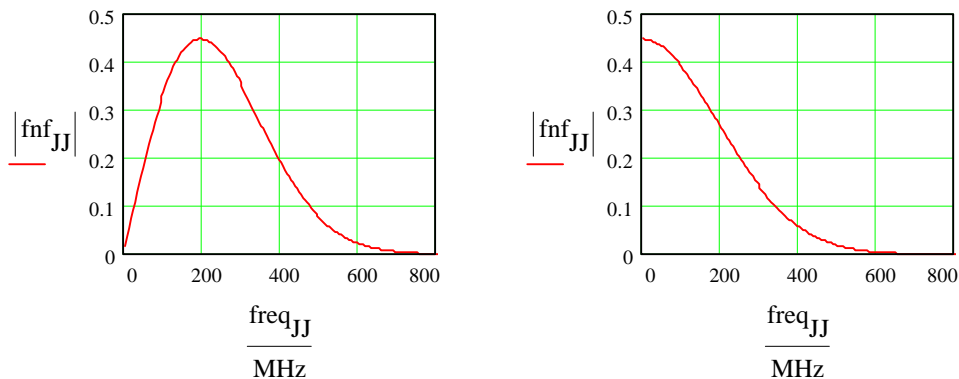


Figure 3.3. Frequency spectrum of the voltage waveforms (left: bipolar pulse, right: unipolar pulse).

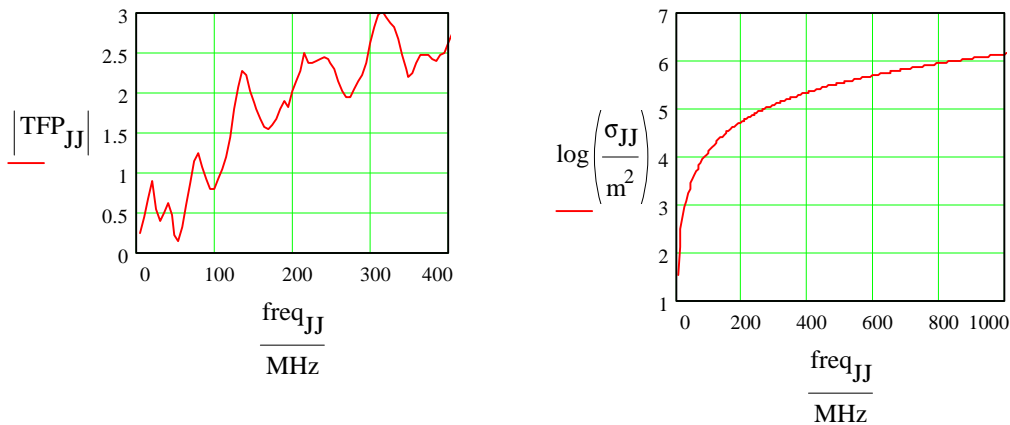


Figure 3.4. Antenna transfer function (left) and the cross section of a flat metal plate with dimensions of 10 m by 10 m.

An existing antenna which may be used for this work is a large TEM horn with flared aperture plates and a high-voltage inline coaxial ‘zipper’ balun as the input section. It has a transfer function as shown in figure 3.4. This was developed by measuring two time domain waveforms. One was a bipolar voltage pulse created by a custom pulse generator with a +/- 100 V amplitude, and primary spectral content from 50 to 400 MHz. The other was the main radiated E-field, at a range of 8.0 m. The transfer function was then formed by the complex ratio of the discrete Fourier transform of the radiated field divided by the transform of the input excitation voltage. The cross section (in Air) of the target (a metal plate 10 m by 10 m) also increases with frequency (see figure 3.4). Because the antenna transfer function and the target cross section are larger at higher frequencies, the unipolar pulse will have less efficiency than the bipolar pulse. It is tempting to use waveforms that have very high frequency components. On the other hand, the attenuation by the soil is larger at higher frequencies. Figure 3.5 shows attenuation for dry sand and San Antonio Clay Loam with a water content of 5%.

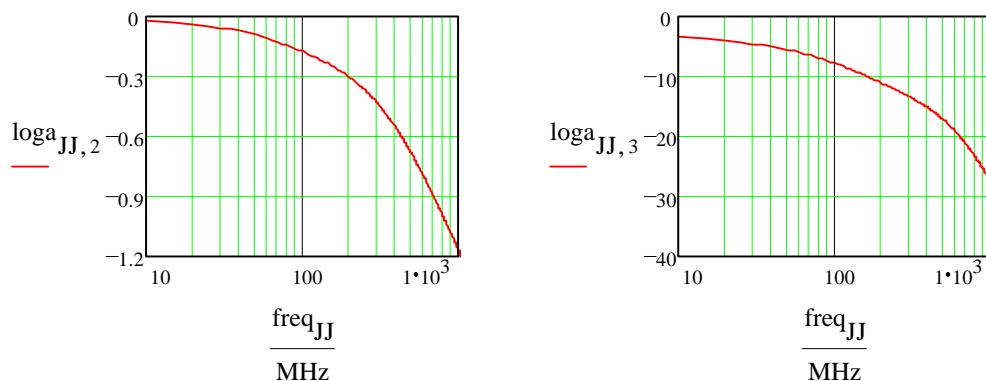


Figure 3.5. The log of the attenuation versus frequency for a penetration depth of 10 m for dry sand (left) and San Antonio clay loam, 5% water (right).

### 3.2 RESULTS FROM THE MODEL

Using this information we can predict the receive waveform. Figures 3.6 and 3.7 show different receive waveforms for the bipolar and unipolar voltage pulses. Figure 3.6 shows the return from penetration through 10 m of air and 10 m of dry sand. Note that the waveforms are similar to the derivative of the initial voltage pulse. Figure 3.7 shows the same type of results but with San Antonio clay loam with 5% water content (4 m of air, 10 m of soil). The receive functions show two major effects. First, a large attenuation of about  $10^5$  in intensity. Second, a great degree of what looks like dispersion in that the temporal extent of the pulse is now about 15 ns. This last effect is mainly due to the high attenuation of the high frequencies that only allow the low (slow) frequencies to be received.

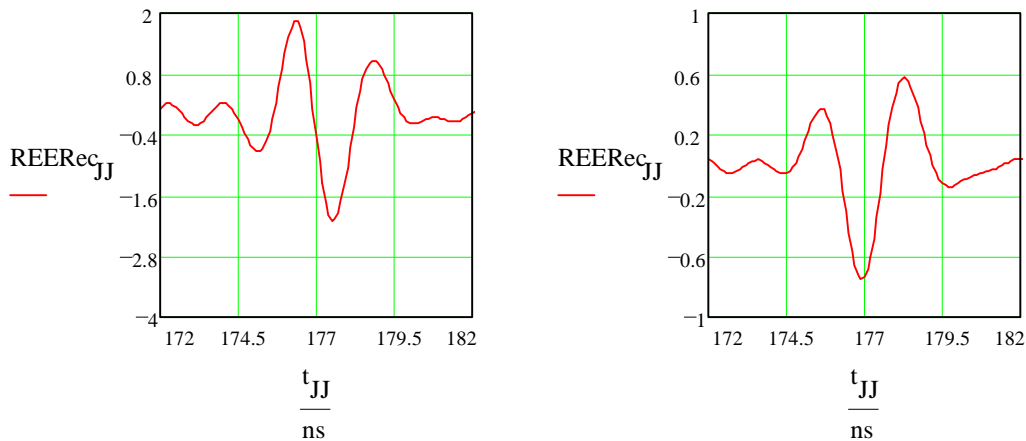


Figure 3.6. The electric field at the transmit site after transmission through dry sand for the bipolar pulse (left) and for the unipolar pulse (right).

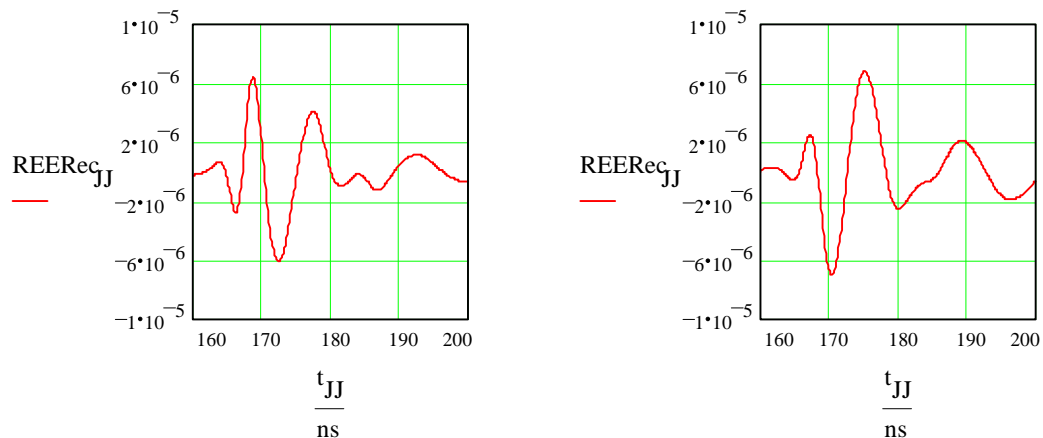


Figure 3.7. The electric field at the transmit site after transmission through San Antonio clay loam, 5% water for the bipolar pulse (left) and for the unipolar pulse (right)..

## 4.0 RADAR TRANSMITTER

A radar transmitter is composed of a modulator that charges a pulse forming line, a pulse forming line that shapes (with the help of switches) the input pulse to an antenna, and the antenna. This chapter describes these three aspects of the radar transmitter we developed and also includes a section on the laser diode/ laser diode drivers we used.

### 4.1 MODULATOR

Two modulators were designed, built and tested: one was an all solid state, SCR-based system and the other was a thyatron-based system. The SCR-based system was developed first because of our desire for an all solid state transmitter. The schematic for the SCR modulator is shown in figure 4.1. The low voltage side of the transformer is a resonantly charged, SCR-based circuit capable of 1 kV output. The transformer had a 150 to 1 turns ratio and was counter-wound. Thus, the voltage on the secondary is of the same polarity as the voltage in the primary. The output of the transformer is connected to the transmission line or pulse forming line using a stack of isolation diodes and a resistor. The need for the diodes, explained in detail in section 2.5, is to improve switch longevity by reducing long duration currents through the switch. Because of the electrical noise produced by the modulator, the modulator was housed in a sealed box with only the transformer, isolation diode stack, and charge resistors outside of the box. We also built a battery-powered AC supply to run the modulator which was used for testing outdoors. Figure 4.2 is a photograph of the system with the SCR-based modulator prior to installation in the sealed box.

Figure 4.3 shows the output voltage from the SCR-based modulator into a 5 M $\Omega$  load. This was measured without the isolation diodes in place using a capacitive monitor. The voltage (y axis) scale is 5.04 kV/ division and the time scale is 10  $\mu$ s/ division. The voltage risetime is about 4  $\mu$ s. The peak voltage was, in this case, 25 kV. The waveform shows a positive pulse with a duration of  $\sim$ 30  $\mu$ s which is followed by a negative pulse (peak negative voltage of -9 kV) with a duration of  $\sim$ 70  $\mu$ s. Because of the need to avoid long duration currents through the switch, we damped the output of the transformer using a 20 k $\Omega$  load across the transmission line. The resulting voltage waveform is shown in figure 4.4. This waveform only has a  $\sim$ 10  $\mu$ s duration positive pulse and a damped (peak negative voltage of -4 kV) negative pulse.

The SCR-based modulator was tested in this configuration to a peak voltage of  $\sim$ 80 kV and a repetition rate of 200 Hz.

The SCR-based modulator was connected to the transmission line, and the line discharged with high gain GaAs switches. First, we tested the system in a unipolar configuration and obtained the appropriate output from the pulse forming line. We then attempted to trigger two switches simultaneously but only one or the other would trigger producing unipolar pulses instead of the desired bipolar pulse. This problem was

resolved, eventually, after much experimentation and testing. One of these tests was to develop a modulator that would charge the line with faster risetime. It was erroneously thought, based partly on previous results, that a faster risetime would result in smaller switch jitter.

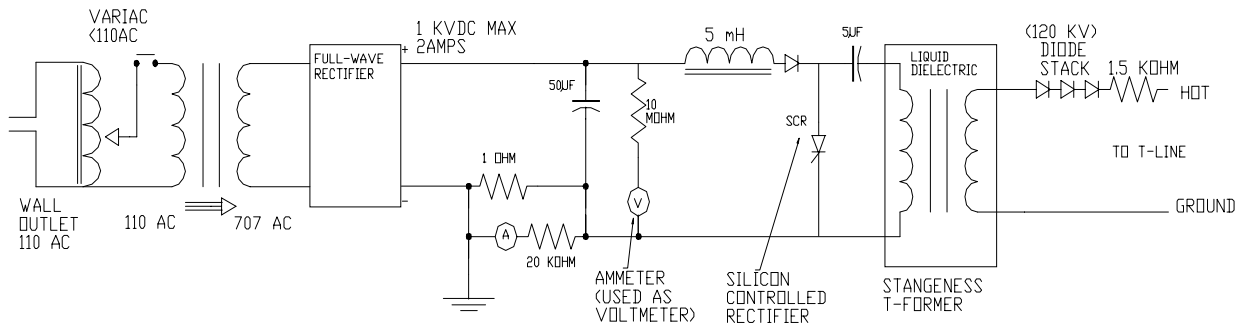


Figure 4.1. Schematic of the SCR-based modulator.



Figure 4.2. Photograph of the system SCR-based modulator prior to installation in the sealed box. The pulse forming line is in the horizontally-aligned tee at the left of the photograph, the transformer is in the vertical container at the center, and the lower voltage circuitry of the modulator is to the right. The large heat sink for the SCR is just to the right of the transformer housing.

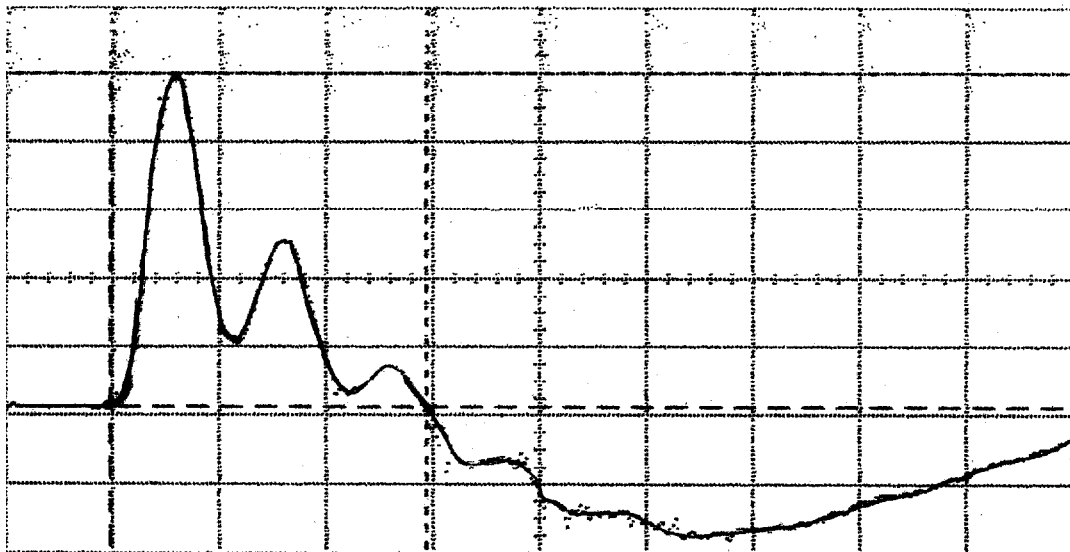


Figure 4.3. The output voltage of the SCR-based modulator into a  $5\text{ M}\Omega$  load. This was measured without the isolation diodes in place using a capacitive monitor. The voltage (y axis) scale is  $5.04\text{ kV/ division}$  with zero voltage at about two divisions from the bottom, and the time scale is  $10\text{ }\mu\text{s/ division}$ . Note that the voltage risetime is about  $4\text{ }\mu\text{s}$ . The peak voltage was, in this case,  $25\text{ kV}$ .

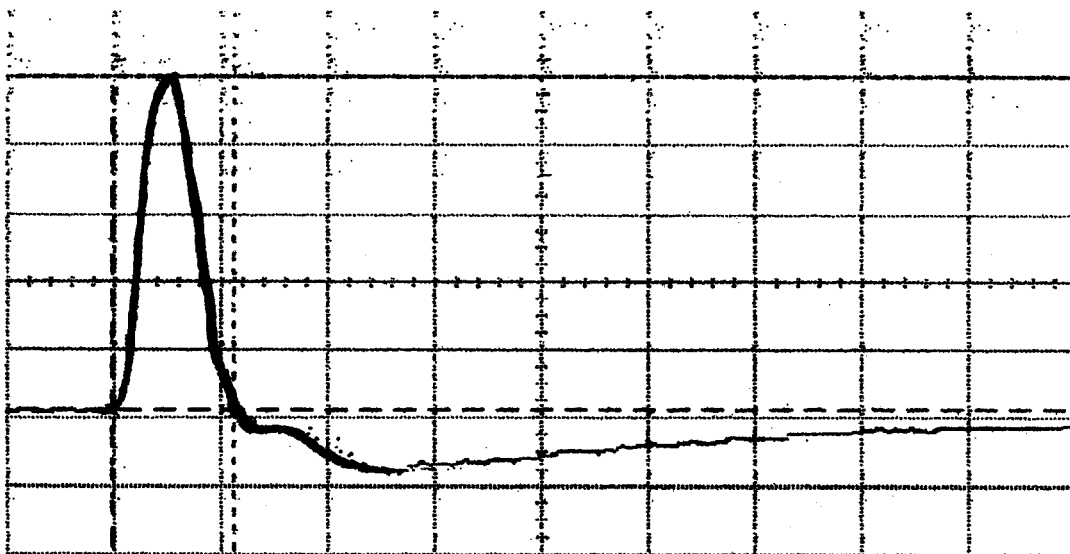


Figure 4.4. The output voltage of the SCR-based modulator into a  $20\text{ k}\Omega$  load that damped the late time ring-down in the previous figure. This was measured without the isolation diodes in place using a capacitive monitor. The voltage (y axis) scale is  $5.04\text{ kV/ division}$  with zero voltage at about two divisions from the bottom, and the time scale is  $10\text{ }\mu\text{s/ division}$ . Note that the voltage risetime is about  $4\text{ }\mu\text{s}$ . The peak voltage was, in this case,  $25\text{ kV}$ .

The schematic for the thyatron-based modulator is, essentially, the same as shown in figure 4.1. The thyatron-based circuit can reach higher voltages in the primary side which allowed for a transformer with a lower turns ratio (6 to 1 instead of 150 to 1). This transformer is not counter-wound so that the polarity of the voltage in the secondary is opposite to that of the primary. The output of the thyatron-based modulator is shown in figures 4.5 and 4.6. The voltage waveform has a much shorter risetime in this system  $\sim 250$  ns compared to  $\sim 4$   $\mu$ s in the SCR-based modulator.

The thyatron-based modulator was tested to a peak voltage of  $\sim 110$  kV and a repetition rate of 800 Hz.

Another advantage of the thyatron-based system is that the pulse forming line stays at high voltage for less time reducing the possibility of corona and switch breakdown. Note that in figure 4.4, the time between the start of the pulse and the next zero crossing is of the order of 10  $\mu$ s. Thus, if we use the isolation diodes to hold the voltage on the pulse forming line until the voltage on the transformer side goes back to zero, the total time between start of pulse and when the switches get triggered is about 10  $\mu$ s. For the thyatron-based system this time is reduced to  $\sim 1.5$   $\mu$ s.

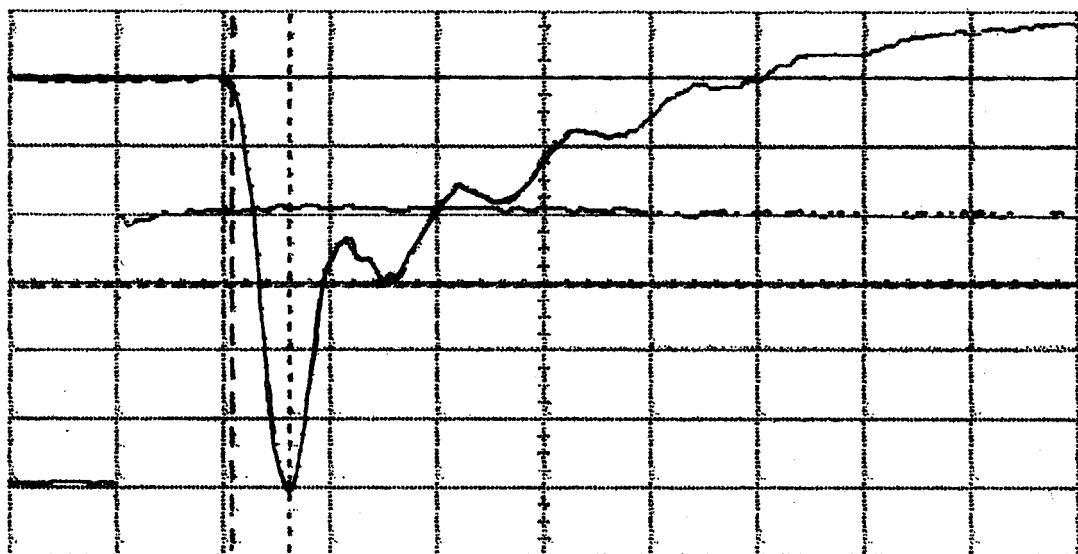


Figure 4.5. The output voltage of the thyatron-based modulator into an open load (the 100 M $\Omega$  of the 1000 to 1 probe used to measure the voltage) and the step trigger for the modulator. The output voltage was measured without the isolation diodes. The voltage (y axis) scale is 5 kV/ division with zero voltage at about one division from the top, and the time scale is 500 ns/ division. Note that the voltage risetime is faster than with the SCR-based modulator ( $\sim 250$  ns vs  $\sim 4$   $\mu$ s). The peak voltage was, in this case, -25 kV. Also shown in the figure is the trigger signal to the modulator (1 V/ division).

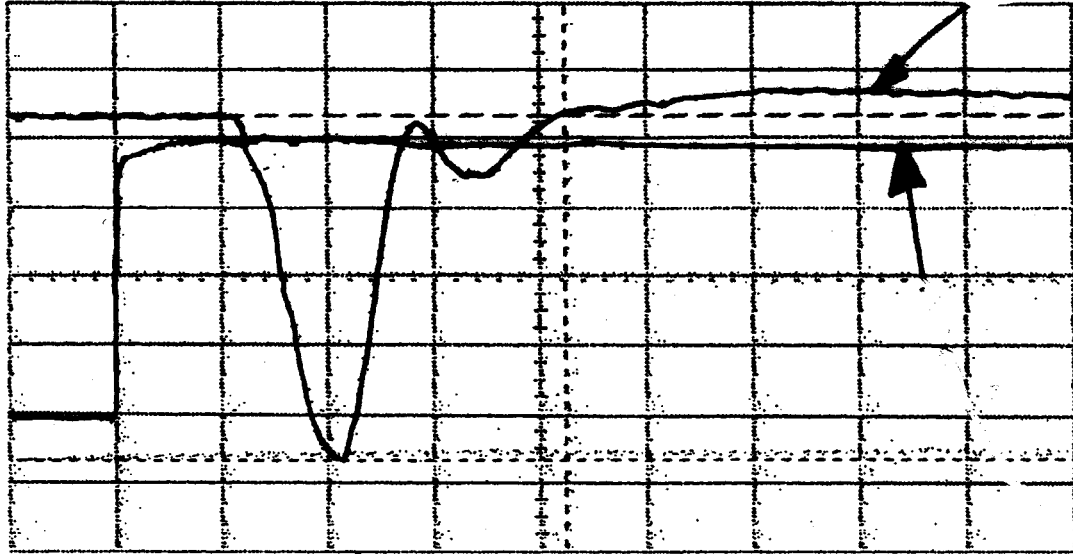


Figure 4.6. The output voltage of the thyatron-based modulator into a  $5\text{ k}\Omega$  load that damped the late time voltage and the step trigger for the modulator. The output voltage was measured without the isolation diodes using a 1000 to 1 probe. The voltage (y axis) scale is  $5\text{ kV/ division}$  with zero voltage at about two divisions from the top, and the time scale is  $500\text{ ns/ division}$ . Note that the voltage risetime is  $\sim 320\text{ ns}$ . The peak voltage was, in this case,  $-25\text{ kV}$ . Also shown in the figure is the trigger signal to the modulator ( $1\text{ V/ division}$ ).

## 4.2 PULSE FORMING LINE

A pulse forming line (PFL) which incorporates two PCSS and a capacitive voltage probe was designed and tested. A schematic of the system is shown in figure 3.1. The PFL is charged by the modulator. If only switch 1 is triggered, the output pulse to the load is a unipolar pulse of the same polarity as the PFL. If both switches are triggered, the PFL produces a bipolar pulse. Figures 4.7 and 4.8 show the PFL's housing and the PFL itself. Note that the two switches are placed horizontally.

We developed several voltage monitors to measure the voltage on the pulse forming line and on the feed to the antenna, the most complicated of which was an integrating capacitive voltage probe. New laser diode array drivers were also built, assembled, and shielded since previous drivers were found to be too susceptible to electro-magnetic interference from the pulser/ transmitter and we needed to assure that the lasers were not being triggered by the modulator or by the first triggering or ringing in the pulse forming line. At one point, jitter in the system was due to false triggering of the lasers.

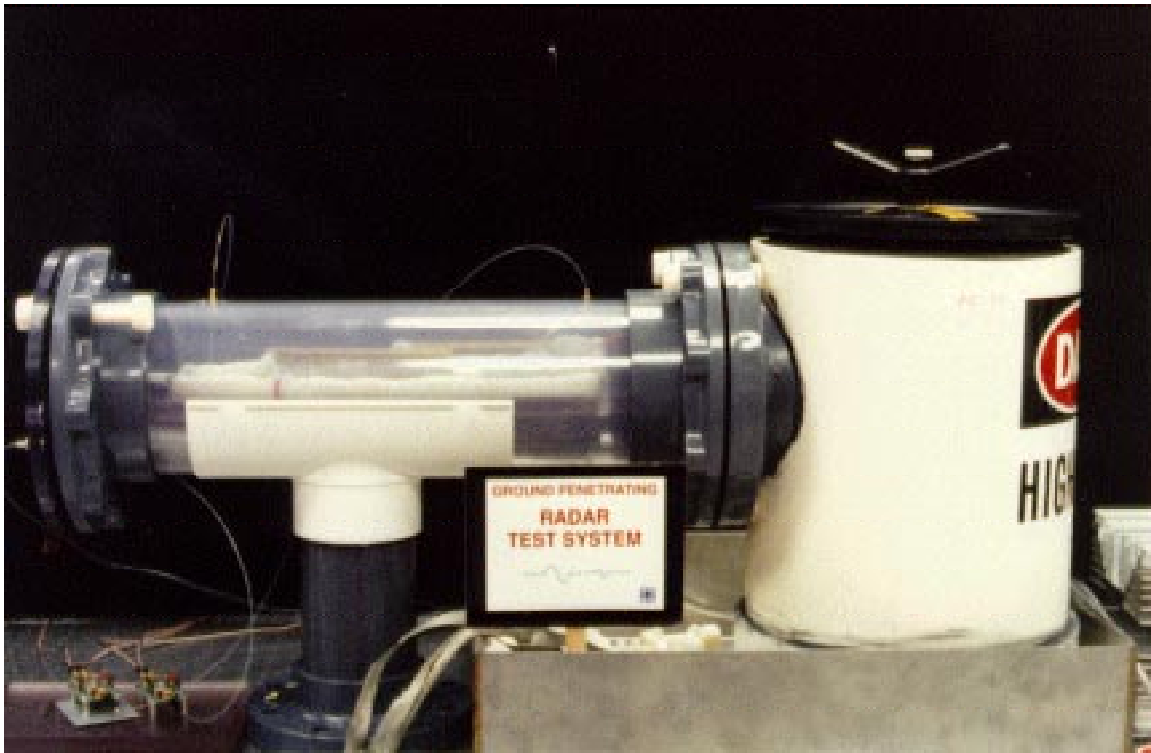


Figure 4.7. The PFL and transformer housings. The PFL is in the horizontally-aligned tee at the left, the transformer is in the vertical container at the right.

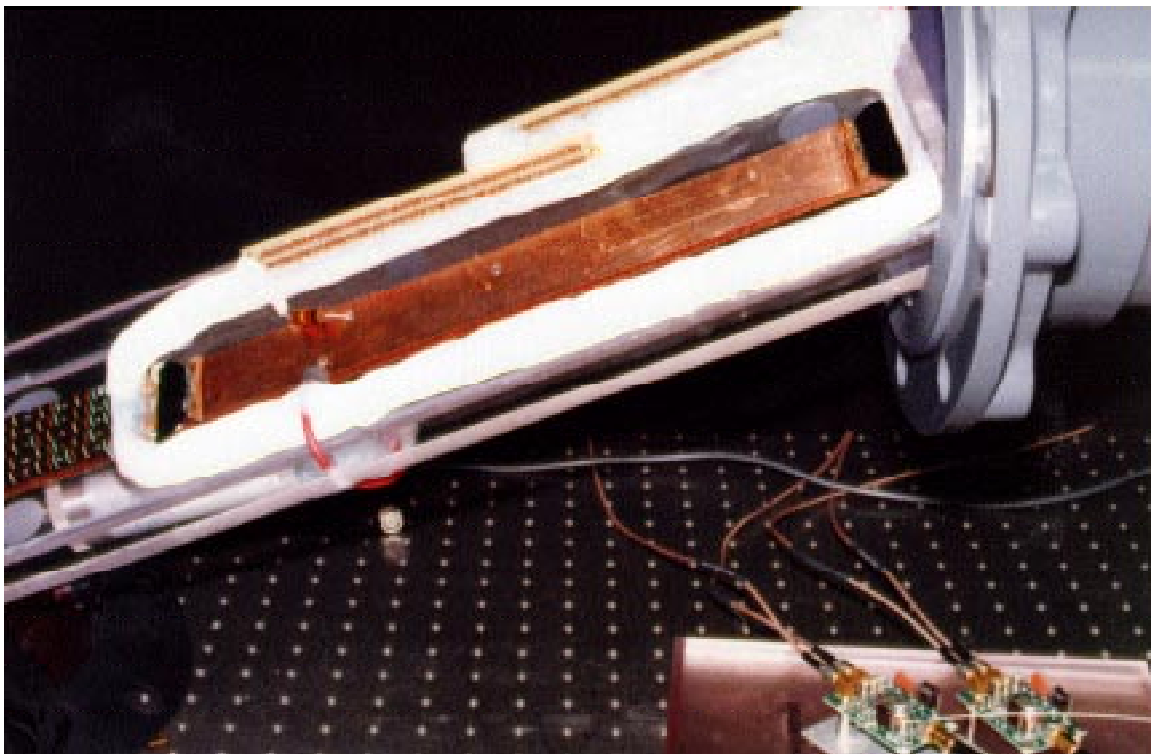


Figure 4.8. The PFL is the copper strip with the two PCSS switches at either end. On the left, is a resistive load/ voltage probe. Two of the laser diodes with their electronic drivers are shown on the bottom right of the photograph.

After the system was built we quickly discovered that we could not easily obtain a bipolar waveform with the PCSS. The problem was that only one or the other switch seemed to trigger even though both of them were being activated. At the start of tests, we only achieved a bipolar waveform once every 10 pulses. By the end of the LDRD we obtained very reproducible waveforms at every pulse. This was achieved through a combination of multiple laser diode triggering and using glass rods as cylindrical lenses to form lines on the switch instead of round spots that are the typical pattern from the optical fibers. The rods result in very prompt firing of the switches with jitter of less than a nanosecond. We also modified the timing of the trigger pulses to the two switches. Instead of firing all the lasers at the same time, we accounted for slight variations in trigger delay between the two switches by triggering one switch slightly earlier than the other one.

The modulator and pulse forming lines were tested with a resistive load. The waveform corresponding to the voltage on the load is shown in figures 4.9 and 4.10 for the unipolar and bipolar pulses, respectively.

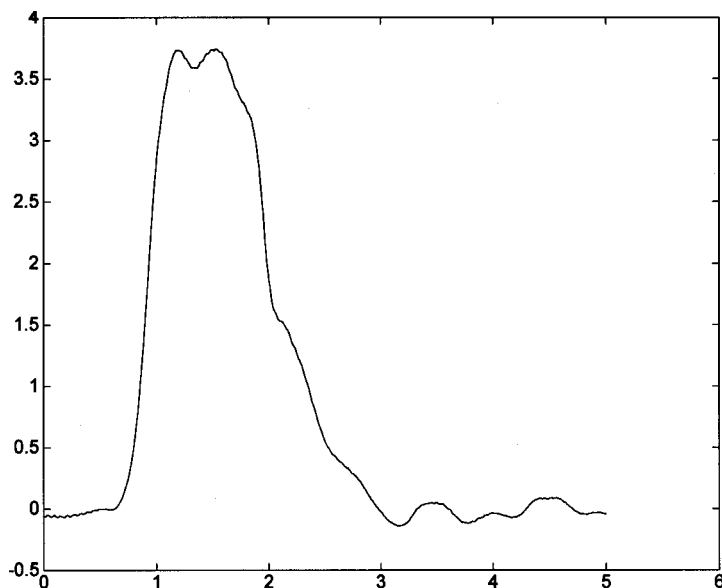


Figure 4.9. The voltage on the load for a unipolar pulse at 60 kV charge. Peak voltage is 21.7 kV, risetime is 1.3 ns, and the pulse width is 4.8 ns, which results in 175 MHz for the bipolar pulse. **The time scale is 5 ns per division.**

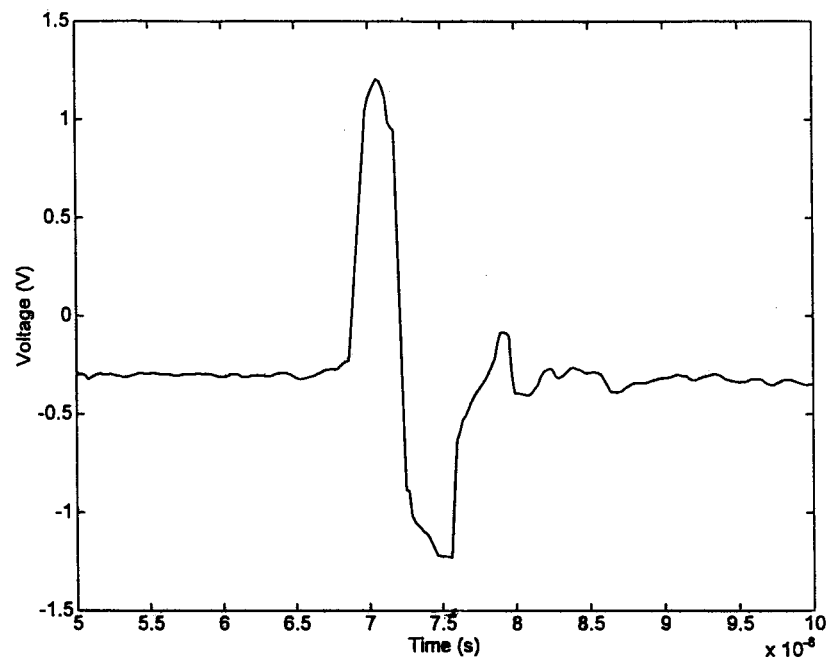


Figure 4.10. The voltage on the load for a bipolar pulse at 75 kV charge. Peak voltage is 31.2 kV, risetime is 113 ns, and the full width of the first (positive) pulse is 3.8 ns. A single cycle with a period of 7.6 ns has a center frequency of 110 MHz. The time scale has a total span of 50 ns.

### 4.3 LASER DIODE ARRAYS AND ELECTRONICS

In this LDRD we used small laser diode arrays to trigger the switches. These were purchased from Laser Diode Inc. (model CVD-167F) and consisted of an array of three laser diodes that are hard coupled to a fiber optic. Their wavelength is around 880 nm. Previous studies at Phillips Lab show that this is the best wavelength to use in terms of the sensitivity of the switches to this light. The pulse duration was 15 to 20 ns. Figure 4.11 shows the laser pulse intensity as a function of time. The total laser energy in each pulse is measured to be about 0.6  $\mu\text{J}$  at the end of the 300  $\mu\text{m}$  fiber. The electronics that power this laser are built at SNL. In this case a single avalanche transistor is switched to deliver a pulse to the array. The package, shown in figure 2.2, measures 2" by 2" by 1". The package requires a voltage of 400 V dc and a trigger. We are now using a small box that contains a dc power supply and a trigger generator to provide the inputs to the package. The power supply and trigger generator in the box are respectively about 3" by 1" by 1.5" (most of which is a dc to dc converter powered by 8 V) and 3" by 2" by 1". This laser can be used repetitively at up to 1 kHz. Thus, the total size of a package of a laser diode array, the electronics, power supply, and trigger generator is less than 15 cubic inches.

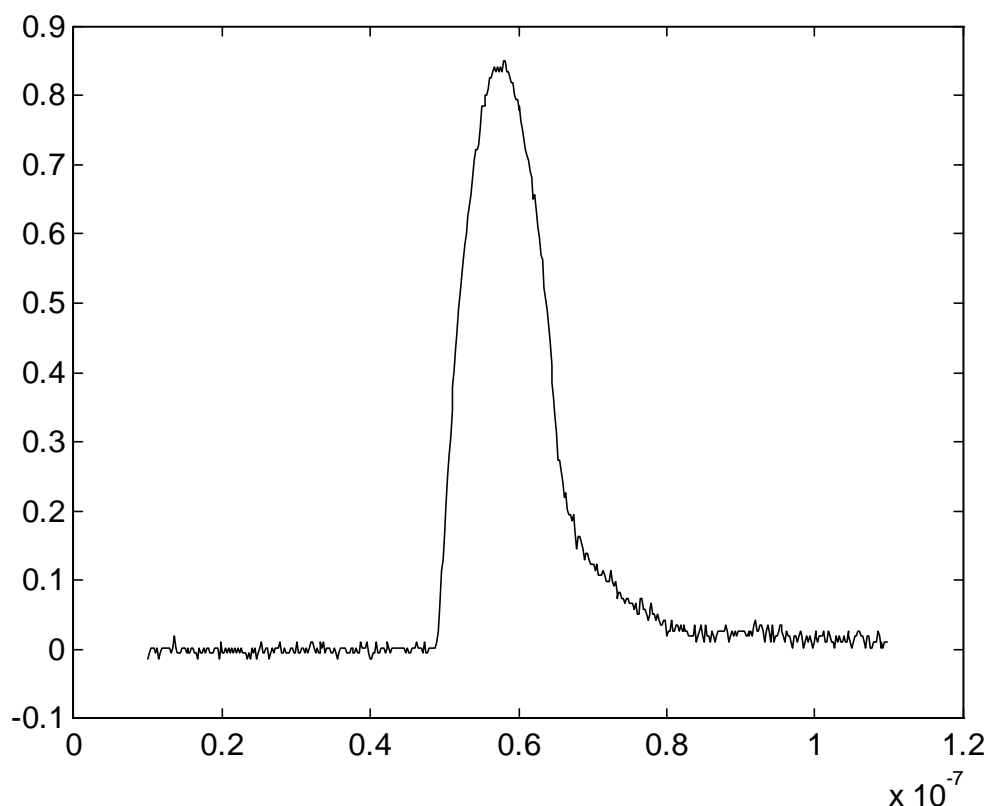


Figure 4.11. The output of the laser diode array. The risetime in this particular waveform is 5 ns and the full width at half maximum is 13 ns. This laser diode array operated at 885 nm and had an output energy (from the fiber) of 0.58  $\mu\text{J}$ .

#### 4.4 ANTENNA AND IMPEDANCE MATCHING SECTION

An existing antenna was tested at low voltages to determine its characteristics, especially at low frequencies. A photograph of the antenna is shown in figure 4.12. We used different techniques (frequency-domain and time-domain) to characterize both the input reflection and the transmitting/radiating performance of the antenna. Time domain reflectometer (TDR) data of the antenna is shown in figure 4.13. Part of the TDR is not relevant to the antenna itself and shows the TDR return from a zipper balun which was used to convert the cylindrical geometry of the 50  $\Omega$  cable to the parallel plate geometry of the system. In the figure, the antenna per se starts at the “input of flat-plate section” label. Its input match is best at 50  $\Omega$ . In the figure, the effect of the flares is visible close to the end of the graph where the impedance starts to rise abruptly. The surge impedance measured by TDR (Voltage/Current) eventually approaches infinity when the wave reaches the end of the antenna (since the current is zero).

The transfer function of the antenna was shown in figure 3.4 and discussed in that chapter. The transfer function has a low frequency roll-off of about 70 MHz (meaning that the antenna does not radiate effectively below 70 MHz). The antenna acts as a derivative antenna almost exclusively. Figure 4.14 shows a comparison of a radiated E-field and the derivative of the input to the antenna. Because of these low voltage tests, we modified the design of the pulse forming line to have 50  $\Omega$  impedance and for it to produce a bipolar pulse with a 5 ns period (so that its peak spectral content is at 200 MHz (the frequency roll-off)). We also built and calibrated a voltage divider to measure the voltage in the antenna (at the feed point).

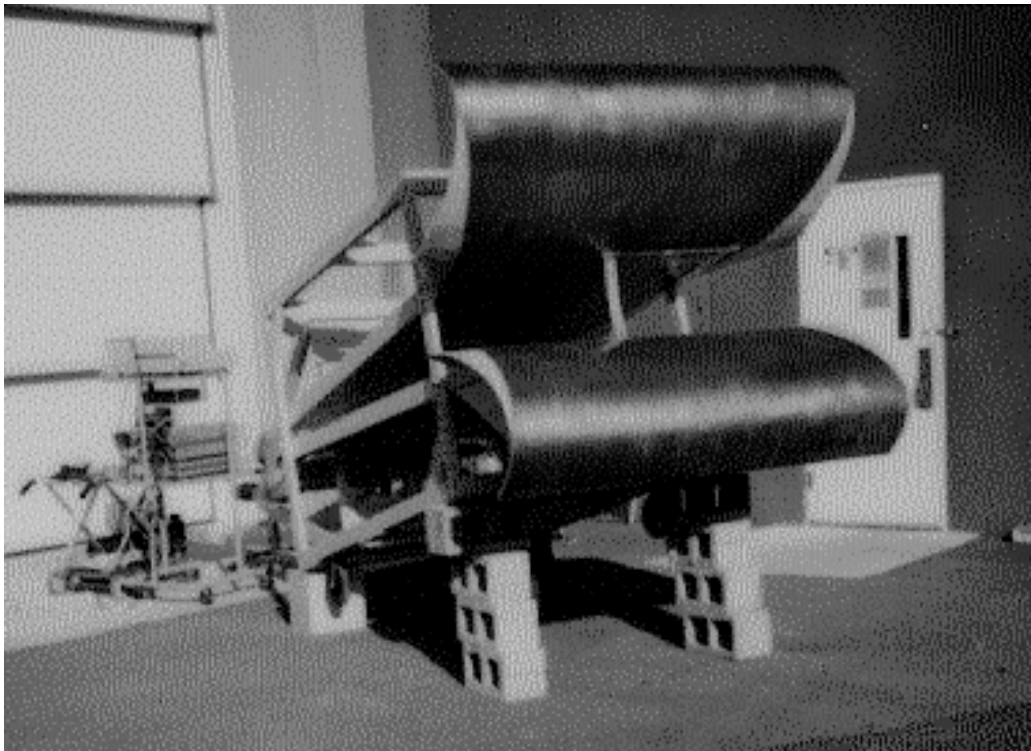


Figure 4.12. The antenna. For scale, note the door behind the antenna.

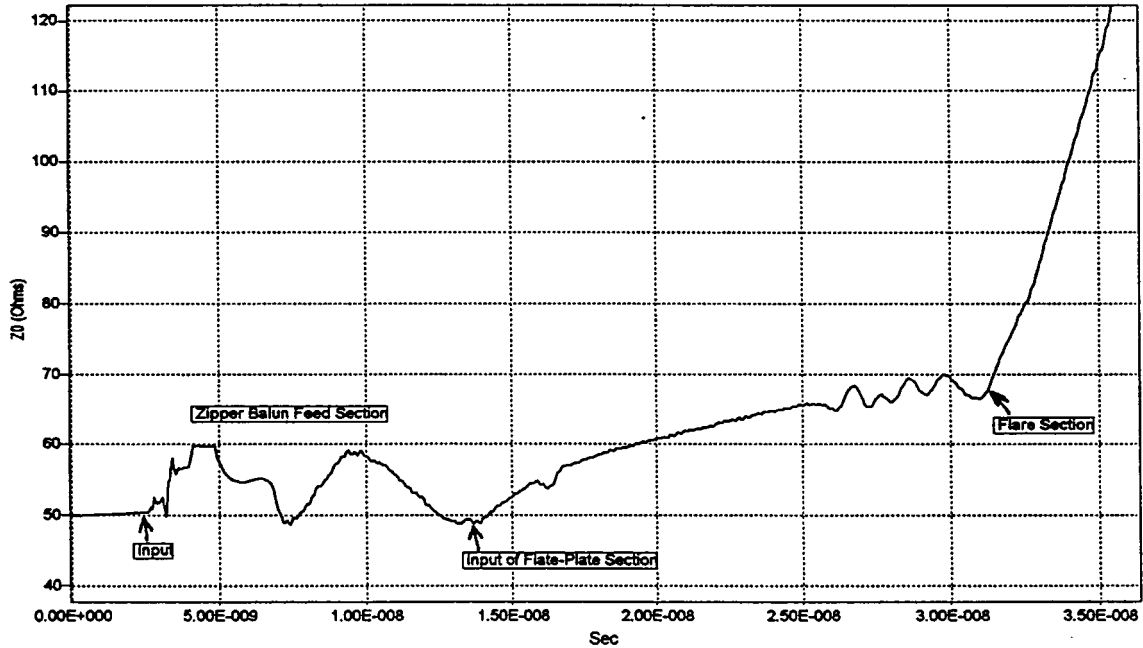


Figure 4.13. Time domain reflectometer data of the antenna using a zipper balun to convert the cylindrical geometry of the  $50 \Omega$  cable to the parallel plate geometry of the system. The antenna per se starts at the “input of flat-plate section” label. The flares at the end of the antenna start close to the end of the graph.

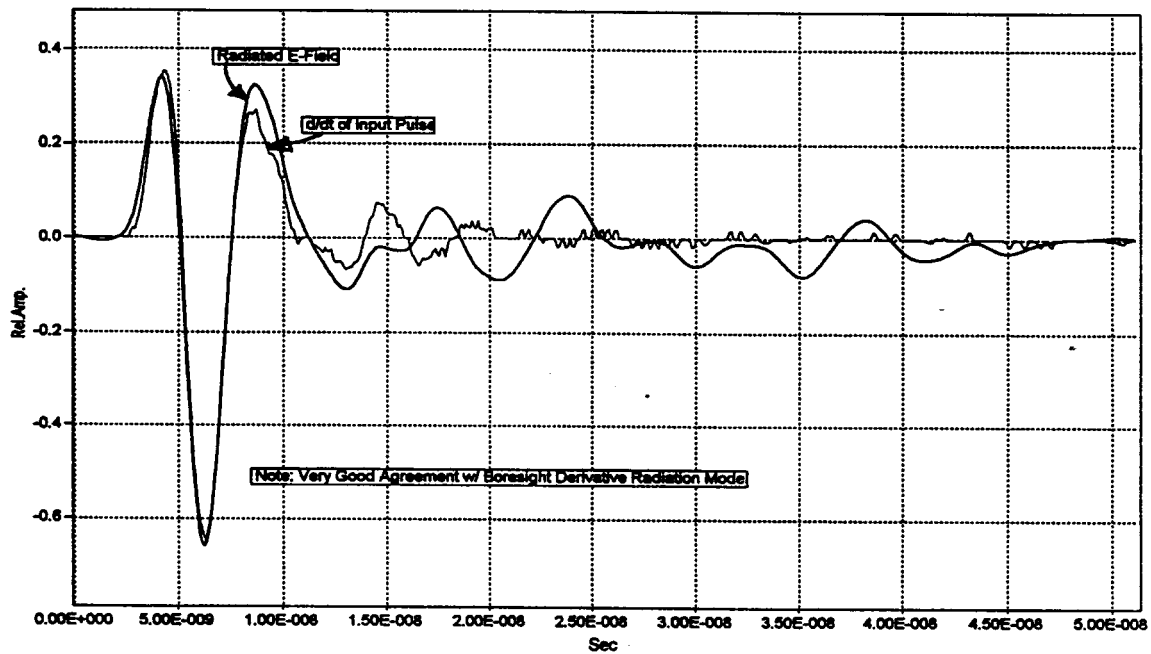


Figure 4.14. Overlay of the measured radiated E-field and the derivative of the input pulse to the antenna.

The receive antenna is a crucial part of this LDRD. Making measurements of antenna response characteristics in the VHF range is well known to be a difficult task. We tested a D-dot antenna and a resistively-loaded TEM horn as receive antennas. The D-dot antenna has good frequency response that extends to very low frequencies but it lacked sensitivity and, thus, the data was too noisy. An alternative was to use the previously calibrated TEM horn. This antenna was built for transient/ time-domain receiving applications such as this one prior to this LDRD. It was designed to produce an output voltage proportional to the incident field. It has a very low dispersion design, discrete resistor loading of the aperture to reduce late- time undershoot of the receiving impulse response, and a broadband matching section. It was calibrated by comparing its output with a precision D-dot receiving antenna (at Sandia) and using a time- domain monocone/ ground plane antenna range (at NIST by Dr. A. Ondrejka). It was designed to have a bandwidth of roughly 100 MHz to 7 GHz, but has an upper roll-off (-3 dB) frequency of only 2.75 GHz (adequate for these experiments). The pass-band of the receiving antenna has an effective height of 2.0 cm averaged over the ~75 MHz to 2 GHz range. Unfortunately, these calibration procedures were carried out at facilities which did not provide the most desirable information in the operating band of the pulser. Regardless, the low frequency roll-off of this antenna (75 MHz) is not as low as we would like (30 MHz). Given that the low frequency roll-off of the transmit antenna is 70 MHz, the roll-off of the receive antenna is barely acceptable.

Once the modulator, pulse forming line and antenna were built and tested individually, the system was assembled and tested as a transmitter. At this time we observed that the system was producing late time ringing: the initial pulse that was sent from the pulse forming line to the antenna was not radiated in its entirety and part of it was reflected back to the pulse forming line and eventually radiated at late times. Figure 4.15 shows the ringing as measured by the voltage monitor at the feed of the antenna. These later pulses are a problem when the receiver is placed adjacent to the antenna since the pulse that arrives from the target may be coincident in time with the late time ringing and may be masked by it. The main reason for the ringing is due to frequency mismatch between the pulser (in the unipolar configuration) and the antenna. The unipolar waveform has peak frequency content at 0 Hz and the antenna is not an effective transmitter at frequencies below 70 MHz. Thus we expected to see ringing in the pulser-antenna system, but it did not necessarily have to be radiated. The radiated waveform shows that this ringing does result in a transmitted pulse with after pulses that last about 200 ns (see section 5). We reduced this late time ringing in two different ways. As demonstrated in figure 4.15, one way was to use the bipolar waveform instead of the unipolar pulse due to a better match with the antenna of the former due to its higher frequency content.

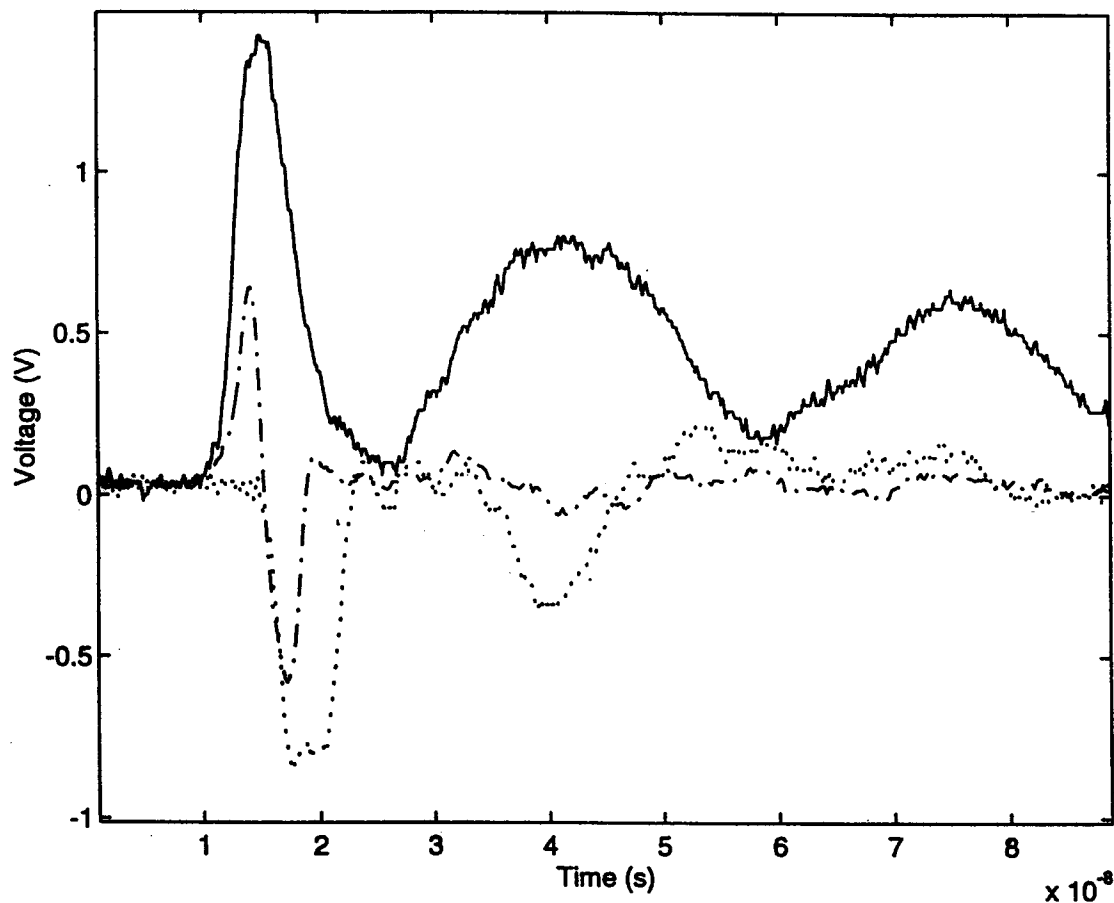


Figure 4.15. The voltage measured at the feed of the antenna for three different PFL output pulses: a positive unipolar pulse (solid line), a negative unipolar pulse (dotted line), and a bipolar pulse (dash-dot line). Note that both unipolar pulses show a second pulse about 25 ns from the initial pulse. This ringing is due to the pulse reaching the antenna opening and reflecting back to the monitor.

We also reduced the ringing in the antenna by using an impedance matching section to connect the pulse forming line to the antenna. The PFL ends with two copper strips of 1.5" width separated by 1/2" Lexan. This was connected to the start of the antenna which was also at 50  $\Omega$  but in air resulting in two plates that were 3" wide separated by 1/2" of air. It was felt that the abrupt change in width was not desirable, thus the impedance matching section was made with a gradual change in the width by tapering the amount of Lexan between the plates. This matching section was adjusted by using TDR data to obtain 50  $\Omega$  impedance throughout the transition.

## 5.0 SYSTEM AND TARGET TESTS

This section summarizes the performance of the system.

### 5.1 SYSTEM TESTS

The pulser-antenna system was set up on the East side of Building 963, in Area IV and we radiated following a protocol that meets the requirements of the Sandia Frequency Coordinator by informing the Kirtland Frequency Surveillance Station that we are about to radiate. Radiated waveforms were measured in a variety of configurations.

As pointed out in the last section, the generation of unipolar pulses into the antenna results in ringing within the transmitter and this ringing is transmitted out of the antenna. Figure 5.1 shows the voltage monitor in the feed section of the antenna and the transmitted pulse measured at a distance of 20' from the antenna with the integrating receive antenna. The pulse into the antenna is a unipolar pulse which shows reflections that are 28 ns apart. The timing of these reflections, and their polarity, is consistent with the reflections arriving at the switches when the switches are in their off state. That is, the PCSS is triggered by the laser diode, the unipolar pulse is launched into the antenna, and by the time the pulse reflects off the front of the antenna and returns to the switch, the switch is no longer conducting.

The received waveform, shown in figure 5.1 is the derivative of the initial pulse (a bipolar pulse) followed by considerable after pulses. These after pulses could be due to the ringing, to ground bounce, and to reflections from nearby structures. It was determined that the primary cause of the after pulses was the ringing in the antenna. As mentioned in the previous section (see figure 4.17), the use of a bipolar pulse as input to the antenna greatly reduces the ringing within the antenna. Thus, antenna characterization proceeded with the bipolar pulse into the antenna. For comparison, figure 5.2 shows the voltage monitor in the feed section of the antenna and the transmitted pulse measured at a distance of 20' from the antenna.

We measured the antenna pattern and the radiated fields as a function of distance. The antenna pattern, shown in figure 5.3, is highly directional. It was measured at a radius of 20 feet although not behind the antenna aperture (it was plotted as 0 in the figure, even though some back lobes may be present). The half power occurs at about +/- 18 degrees (full width at half maximum is 36 degrees). There are lobes at about 56 degrees. The electric field versus distance, shown in figure 5.4, was measured and is 1.3 kV/m at 20 feet, 0.34 kV/m at 40 feet, and 64 V/m at 100 feet for a charge voltage of 12 kV. Figure 5.4 also shows a 1/r dependence. The measured values are in close agreement with 1/r, any deviations from a 1/r dependence are due to taking data in the near field, to ground bounce effects which were partially interfering with the results, or with bandwidth limitations on the receiver.

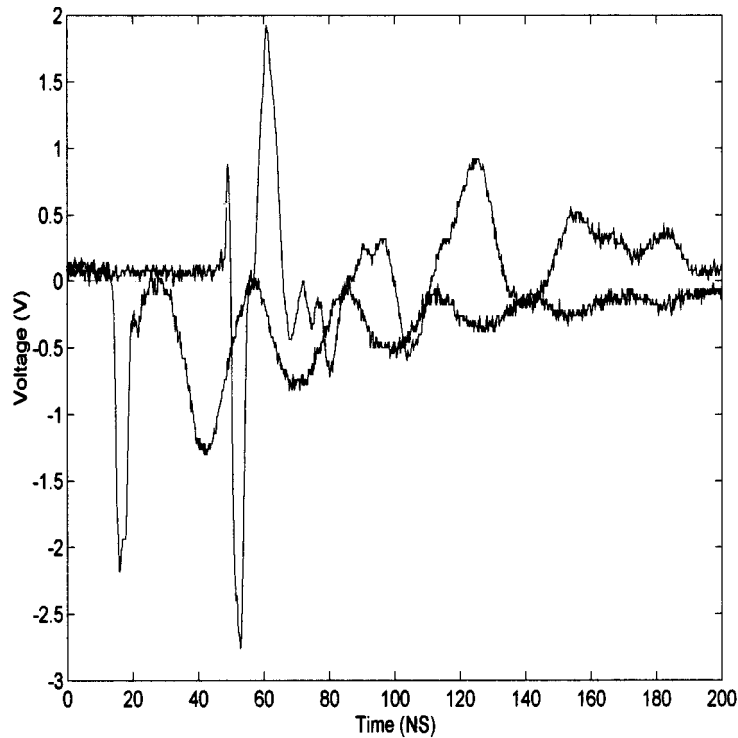


Figure 5.1. This figure shows two waveforms. The first one is the pulse into the antenna, a unipolar pulse. Note that the transmitter rings with a period of about 28 ns. The second waveform is the receive signal at boresight (20' distance) and shows the effect of this ringing.

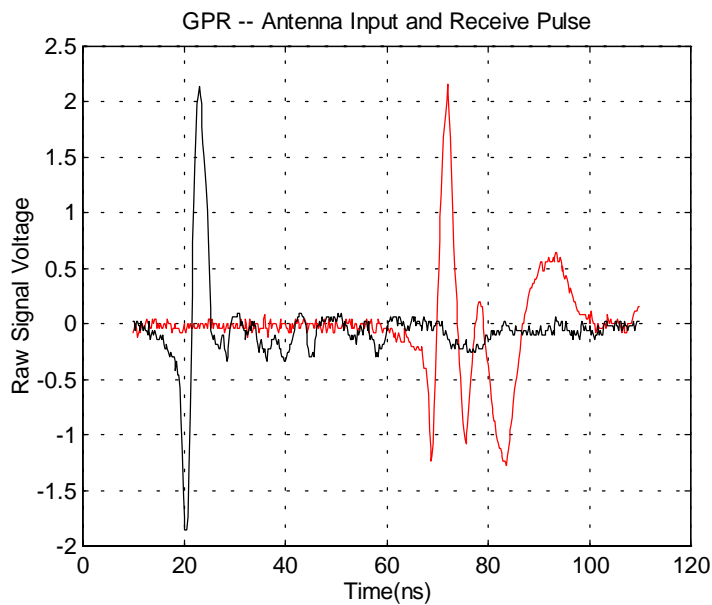


Figure 5.2. This figure shows two waveforms. The first one is the pulse into the antenna, a bipolar pulse. Note that the ringing of the transmitter is much reduced when compared to that of the unipolar pulse. The second waveform is the receive signal at boresight (20' distance).

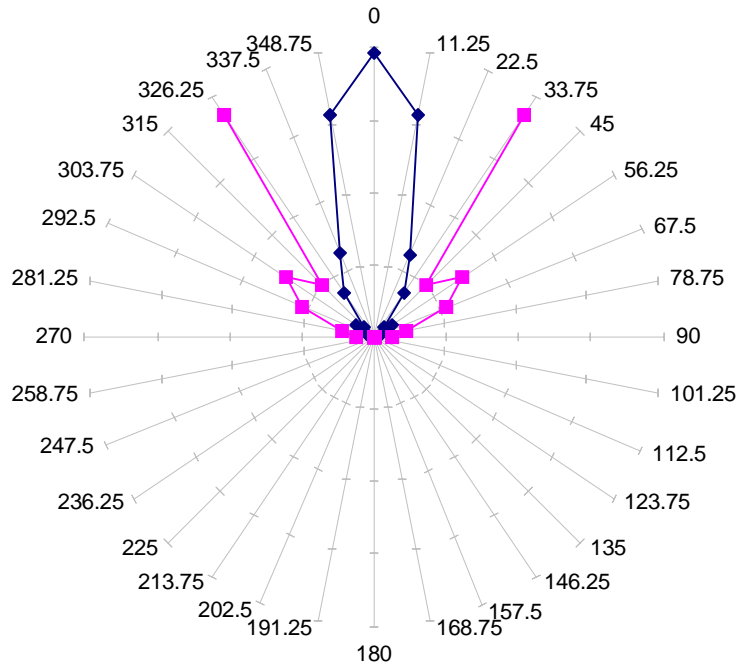


Figure 5.3. Two curves showing the antenna power pattern (the power was not measured behind the antenna aperture and is plotted as 0). One of the curves is shown expanded by a factor of 6 to highlight the lobes at  $56^\circ$ .

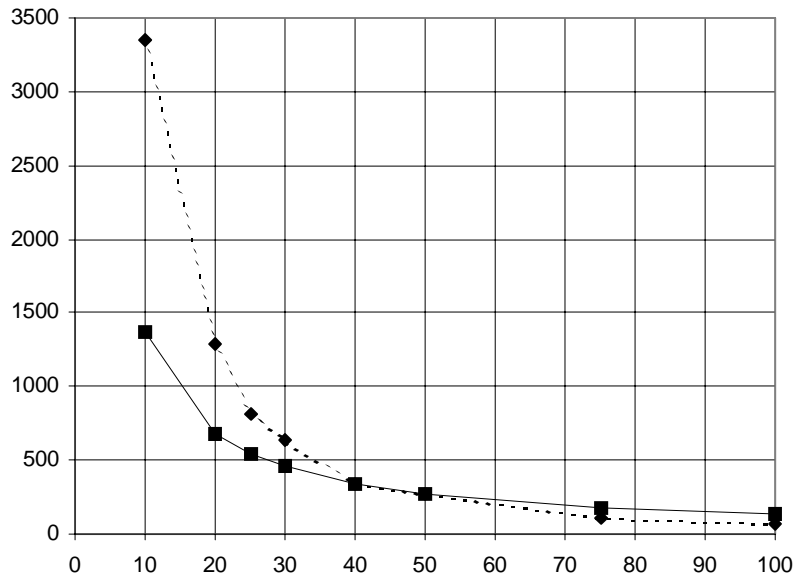


Figure 5.4. Electric field in V/m (◆) as function of distance from the antenna aperture for a charge voltage of 12 kV. A plot of  $1/\text{distance}$ , normalized at 40 feet is also included (■).

## 5.2 TESTS WITH UN-OBSCURED TARGETS

After the system was characterized, we measured the return waveform from a target in air: We measured return waveforms from a 4' by 8' metal plate. The best results were obtained with the plate at  $45^\circ$  relative to the direction of the incoming electromagnetic wave and the receiver at 90 degrees. This reduced the effects of antenna ringing relative to the case when the receiver was co-located with the transmit antenna. The target was at a distance of  $\sim 20'$  from the antenna (boresight) and the receiver at  $\sim 20'$  from the target. Figure 5.5 shows the voltage input to the antenna and the receive (reflected) signal. In comparison to figures 5.1 and 5.2 the big difference is that the first signals that arrive at the receiver are not the boresight signals. There is a weaker signal that is transmitted at  $45^\circ$  and arrives at the receiver prior to the signal that is reflected off the target.

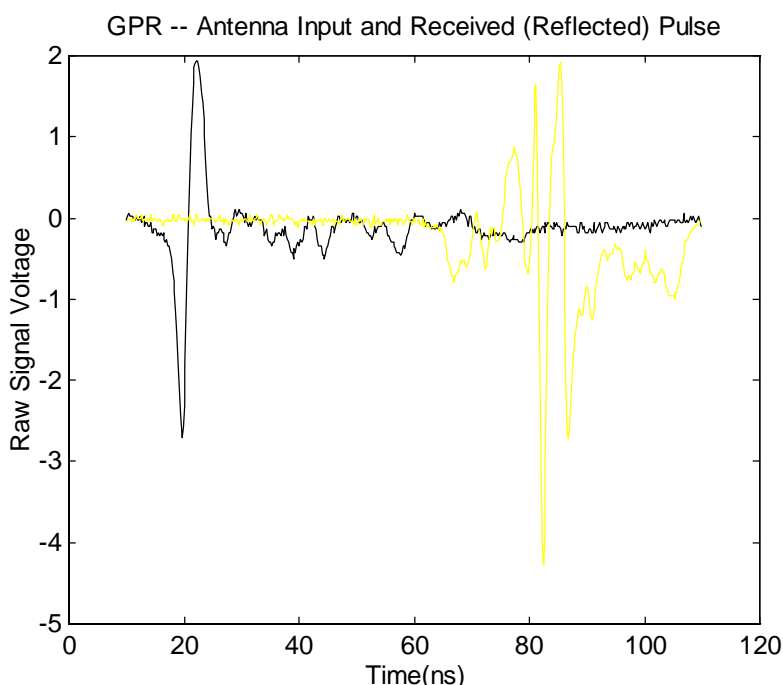


Figure 5.5. This figure shows two waveforms. The first one is the pulse into the antenna, a bipolar pulse. The second waveform is the receive signal from a 4' by 8' metal plate. The target was  $\sim 20'$  from the antenna, inclined at  $45^\circ$  from boresight, so that the reflected wave was aimed at the receiver.

A better demonstration of the ability of the system to observe targets is to use background subtraction. Figure 5.6 shows the received signal with no target. The only signals received are  $45^\circ$  emission from the antenna and reflections from nearby objects. Figure 5.7 shows the signal with the target. Figure 5.8 shows the subtraction of the two signals.

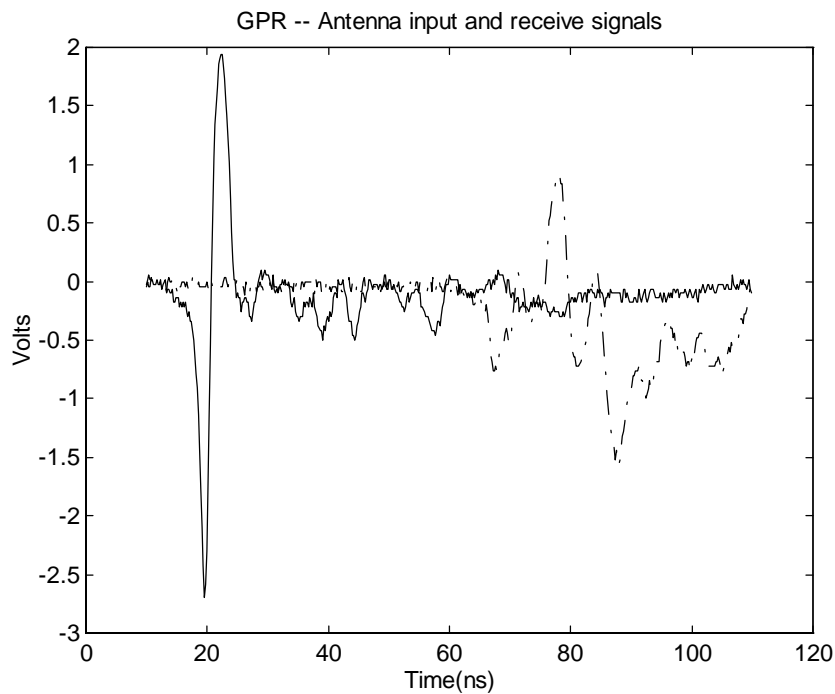


Figure 5.6. The solid line shows the pulse into the antenna. The broken one is the receive signal with no target to reflect the pulse to the receiver. It is the same geometry as in figure 5.5 and 5.7 but there is no target.

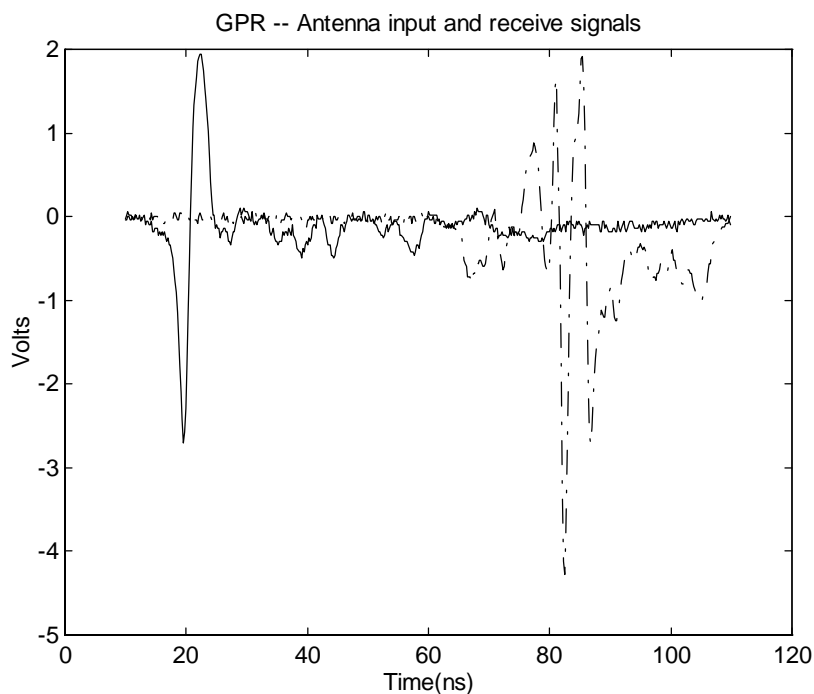


Figure 5.7. The solid line shows the pulse into the antenna. The broken line is the receive signal from a 4' by 8' metal plate. It is the same geometry as in figure 5.6 but there a target.

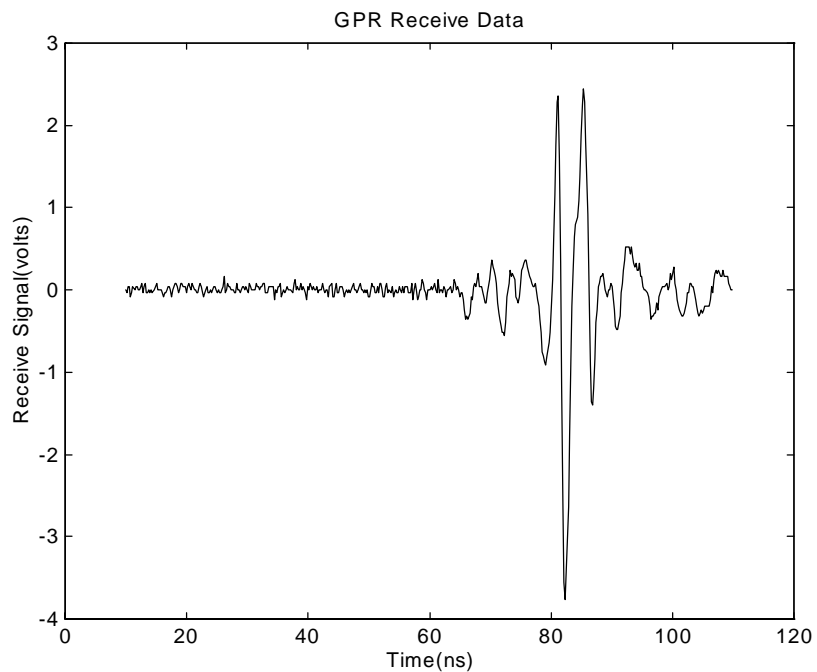


Figure 5.8. The difference in the received waveforms with and without a target.

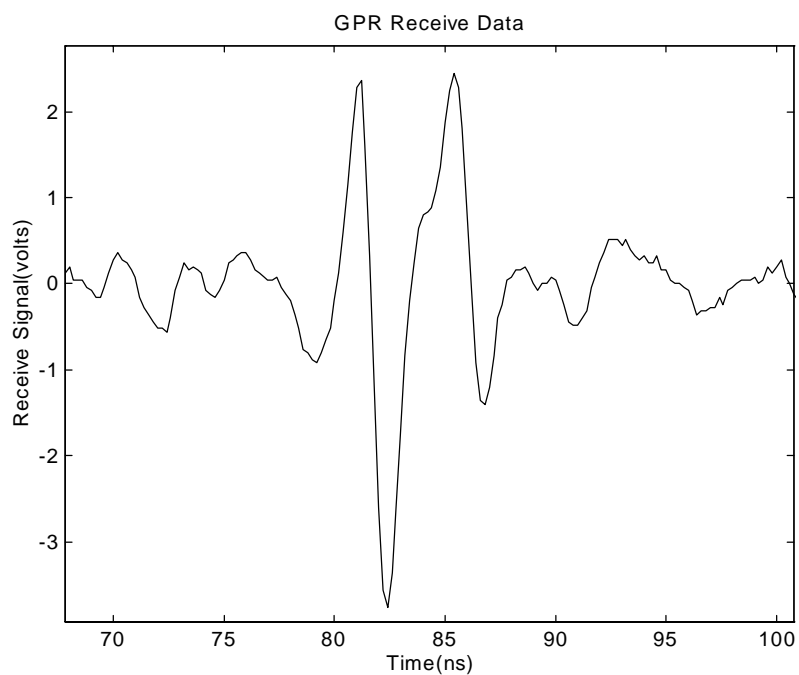


Figure 5.9. The difference in the received waveforms with and without a target in an expanded time scale.

### 5.3 PENETRATION THROUGH CONCRETE

We measured penetration through concrete, and return waveforms from targets behind concrete walls. First, we placed a receiver behind large concrete blocks used for radiation shielding: each block is 3' by 2' by 6' . We used a total of 6 blocks and a metal plate on top to reduce the effect of the wave that travels around the blocks. Figure 5.10 shows the setup. The blocks were at 100' from the antenna. The signal was measured with the receiver inside the block structure and just outside. Figures 5.11 and 5.12 show the waveforms. Note that the signal amplitude was reduced by a factor of only 2.8.

We also placed a 4' by 8' metal-plate target behind the wall of building 962 and measured returns. Measurable penetration signals were observed.

Finally, we placed the transmitter to look for penetration of real soil. We were not able to measure any returns due to two reasons. First, we used the transmit antenna as a receive antenna. The problem with this configuration is that we had a low dynamic range measurement since the monitor had to measure the high voltage pulse into the antenna. The second reason was that recent rains had raised the water content of the soil to 8%.



Figure 5.10. This photograph shows the concrete blocks used for tests of penetration through concrete. The blocks are those used for radiation shielding: 2' thick by 3' high by 6' wide, made from high density concrete. The receiver was placed behind the blocks.

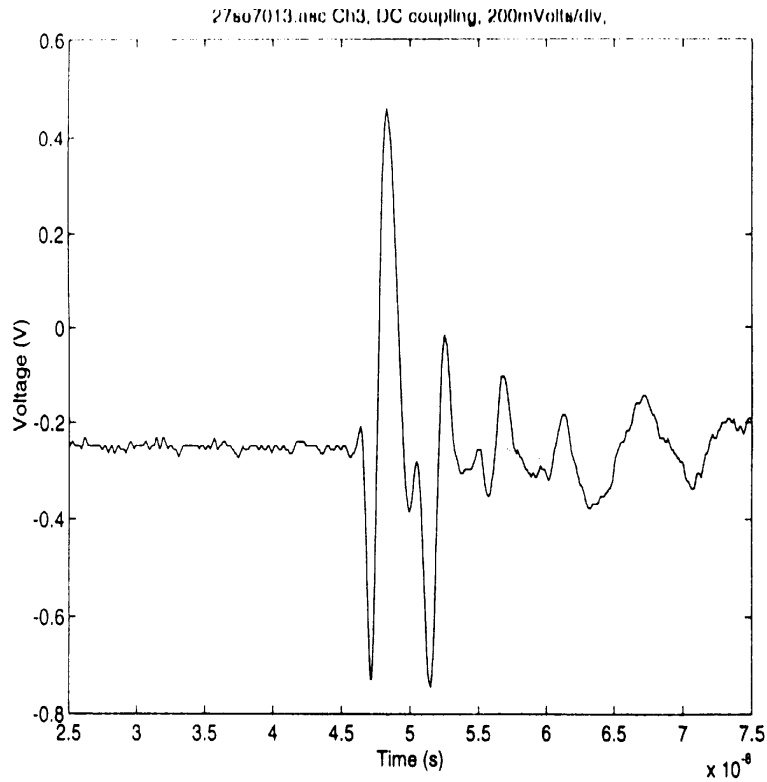


Figure 5.11 The waveform with the receiver to the side of the blocks.

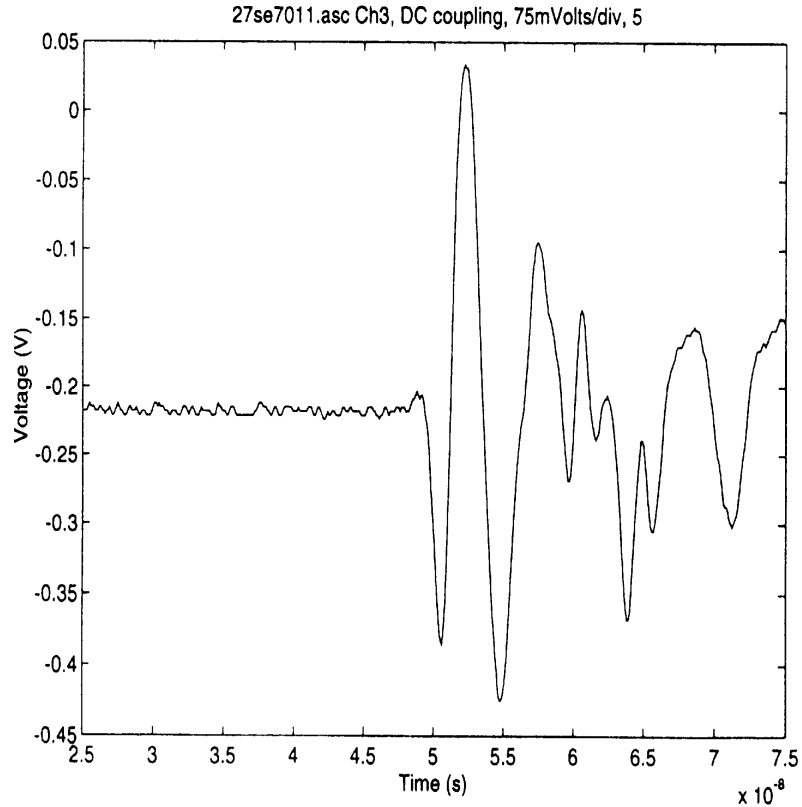


Figure 5.12. The waveform with the receiver behind the blocks.

## 6.0 REFERENCES

- 1) For general references on high gain PCSS technology see the following:
  - a.) IEEE Pulsed Power Conferences, 1985-97 (odd years)
  - b.) IEEE Power Modulator Symposia, 1986-96 (even years)
  - c.) SPIE Optically Activated Switching Conferences I-IV, 1990, 1992, 1993, 1994.
  - d.) F. J. Zutavern, G. M. Loubriel, M. W. O'Malley, L. P. Schanwald, W. D. Helgeson, D. L. McLaughlin, and B. B. McKenzie, "Photoconductive semiconductor switch experiments for pulsed power applications," *IEEE Trans. Elect. Devices*, Vol. 37, No. 12, 1990, pp. 2472-2477.
  - e.) A. Rosen and F. J. Zutavern, Eds., *High-Power Optically Activated Solid State Switches*, Artech House, Boston, 1993, pp. 245-296.
  - f.) G. M. Loubriel, F. J. Zutavern, H. P. Hjalmarson, R. R. Gallegos, W. D. Helgeson, and M. W. O'Malley, "Measurement of the Velocity of Current Filaments in Optically Triggered, High Gain GaAs Switches", *Applied Physics Letters*, Vol. 64, No. 24, 13 June, 1994, pp. 3323-3325.
  - g.) G. M. Loubriel, F. J. Zutavern, A. G. Baca, H. P. Hjalmarson, T. A. Plut, W. D. Helgeson, M. W. O'Malley, M. H. Ruebush, and D. J. Brown, "Photoconductive Semiconductor Switches," *IEEE Transactions on Plasma Science*, 25, 1997, pp. 124-130.
- 2) References on switch longevity:
  - a) G. M. Loubriel, F. J. Zutavern, A. Mar, M. W. O'Malley, W. D. Helgeson, D. J. Brown, H. P. Hjalmarson, and A. G. Baca, "Longevity of Optically Activated, High Gain GaAs Photoconductive Semiconductor Switches," to be published in *Proceedings of 11th IEEE Pulsed Power Conference*, Baltimore, MD, June 29-July 2, 1997.
  - b) G. M. Loubriel, F. J. Zutavern, A. Mar, H. P. Hjalmarson, A. G. Baca, M. W. O'Malley, W. D. Helgeson, D. J. Brown, and R. A. Falk, "Longevity of Optically Activated, High Gain GaAs Photoconductive Semiconductor Switches," to be published in *IEEE Transactions on Plasma Science*.
- 3) G. M. Loubriel, et al, "High Gain GaAs Photoconductive Semiconductor Switches for Impulse Sources," *Proc. of SPIE Optically Activated Switching Conference IV*, SPIE Vol. 2343, p. 180, W. R. Donaldson, ed., Boston, MA, 1994.
- 4) G. M. Loubriel, M. T. Buttram, J. F. Aurand, and F. J. Zutavern, "Ground Penetrating Radar Enabled by High Gain GaAs Photoconductive Semiconductor Switches," in *Ultra-Wideband, Short Pulse Electromagnetics 3*, A. Stone, C. Baum, and L. Carin, eds., Plenum Press, NY, 1996, pp. 17- 24.
- 5) G. M. Loubriel, F. J. Zutavern, W. D. Helgeson, D. J. Brown, and M. W. O'Malley, "High Gain GaAs Switches for Ground Penetrating Radar", *Proc. 22nd Power Modulator Symposium (IEEE, NY, 1996)*, Boca Raton, FL, June 24-27, 1996, pp. 165-168.

**DISTRIBUTION****INTERNAL DISTRIBUTION**

1314, MS 1060	A. G. Baca
1314, MS 0603	T. E. Zipperian
2674, MS 0328	J. A. Wilder
2674, MS 0328	S. C. Holswade
7585, MS 1148	F. L. Peace
9000, MS 0151	G. Yonas
9232, MS 0820	H. P. Hjalmarson
9300, MS 1165	J. Polito
9301, MS 1165	D. M. Rondeau
9331, MS 1153	D. W. Brown
9331, MS 1153	M. T. Buttram
9331, MS 1153	W. D. Helgeson
9331, MS 1153	G. M. Loubriel
9331, MS 1153	A. Mar
9331, MS 1153	M. W. O'Malley
9331, MS 1153	F. J. Zutavern
9500, MS 1190	D. L. Cook
9512, MS 1188	R. A. Hamil
4916, MS 0899	Technical Library (5)
8940-2, MS 9018	Central Technical Files
12690, MS 0619	Document Processing for DOE/OSTI (2)